




| | |
|----------------------------------|--|
| Publication Year | 2022 |
| Acceptance in OA | 2025-03-08T17:58:16Z |
| Title | The MeerKAT Galaxy Cluster Legacy Survey: I. Survey Overview and Highlights |
| Authors | Knowles, K., Cotton, W. D., Rudnick, L., Camilo, F., Goedhart, S., Deane, R., RAMATSOKU, MPATI ANALICIA, Bietenholz, M. F., Brüggem, M., Button, C., Chen, H., Chibueze, J. O., Clarke, T. E., DE GASPERIN, Francesco, Ianjamasimanana, R., Józsa, G. I.G., Hilton, M., Kesebonye, K. C., Kolokythas, K., Kraan-Korteweg, R. C., Lawrie, G., Lochner, M., Loubser, S. I., Marchegiani, P., Mhlahlo, N., Moodley, K., Murphy, E., Namumba, B., Oozeer, N., Parekh, V., Pillay, D. S., Passmoor, S. S., Ramaila, A. J.T., Ranchod, S., Retana-Montenegro, E., Sebokolodi, L., Sikhosana, S. P., Smirnov, O., Thorat, K., VENTURI, Tiziana, Abbott, T. D., Adam, R. M., Adams, G., Aldera, M. A., Bauermeister, E. F., Bennett, T. G.H., Bode, W. A., Botha, D. H., Botha, A. G., Brederode, L. R.S., Buchner, S., Burger, J. P., Cheetham, T., De Villiers, D. I.L., Dikgale-Mahlakoana, M. A., Du Toit, L. J., Esterhuyse, S. W.P., Fadana, G., Fanaroff, B. L., Fataar, S., Foley, A. R., Fourie, D. J., Frank, B. S., Gamatham, R. R.G., Gatsi, T. G., Geyer, M., Gouws, M., Gumede, S. C., Heywood, I., Hlakola, M. J., Hokwana, A., Hoosen, S. W., Horn, D. M., Horrell, J. M.G., Hugo, B. V., Isaacson, A. R., Jonas, J. L., Jordaan, J. D.B., Joubert, A. F., Julie, R. P.M., Kapp, F. B., Kasper, V. A., Kenyon, J. S., Kotzé, P. P.A., Kotze, A. G., Kriek, N., Kriel, H., Krishnan, V. K., Kusel, T. W., Legodi, L. S., Lehmensiek, R., Liebenberg, D., Lord, R. T., Lunskey, B. M., Madisa, K., Magnus, L. G., Main, J. P.L., Makhaba, A., Makhathini, S., Malan, J. A. |
| Publisher's version (DOI) | 10.1051/0004-6361/202141488 |
| Handle | http://hdl.handle.net/20.500.12386/36550 |
| Journal | ASTRONOMY & ASTROPHYSICS |
| Volume | 657 |

The MeerKAT Galaxy Cluster Legacy Survey

I. Survey Overview and Highlights[★]

K. Knowles^{1,2,3} , W. D. Cotton^{4,3}, L. Rudnick⁵, F. Camilo³, S. Goedhart³, R. Deane^{6,7}, M. Ramatsoku^{2,8}, M. F. Bietenholz^{9,10}, M. Brüggén¹¹, C. Butten⁷, H. Chen¹², J. O. Chibueze^{13,14}, T. E. Clarke¹⁵, F. de Gasperin^{11,16}, R. Ianjamasimanana^{2,3}, G. I. G. Józsa^{3,2,17}, M. Hilton^{1,18}, K. C. Kesebonye^{1,18}, K. Kolokythas¹³, R. C. Kraan-Korteweg¹², G. Lawrie^{6,7}, M. Lochner^{19,3}, S. I. Loubser¹³, P. Marchegiani^{6,20}, N. Mhlahlo⁶, K. Moodley^{1,18}, E. Murphy⁴, B. Namumba², N. Oozeer^{3,21}, V. Parekh^{2,3}, D. S. Pillay^{1,18}, S. S. Passmoor³, A. J. T. Ramaila³, S. Ranchod^{6,7}, E. Retana-Montenegro^{1,18}, L. Sebokolodi², S. P. Sikhosana^{1,18}, O. Smirnov^{2,3}, K. Thorat^{7,22}, T. Venturi¹⁶, T. D. Abbott³, R. M. Adam³, G. Adams³, M. A. Aldera²³, E. F. Bauermeister³, T. G. H. Bennett³, W. A. Bode³, D. H. Botha²⁴, A. G. Botha³, L. R. S. Brederode^{3,25}, S. Buchner³, J. P. Burger³, T. Cheetham³, D. I. L. de Villiers²⁶, M. A. Dikgale-Mahlakoana³, L. J. du Toit²⁴, S. W. P. Esterhuysen³, G. Fadana³, B. L. Fanaroff³, S. Fataar³, A. R. Foley³, D. J. Fourie³, B. S. Frank^{3,22,12}, R. R. G. Gamatham³, T. G. Gatsi³, M. Geyer³, M. Gouws³, S. C. Gumede³, I. Heywood^{27,2,3}, M. J. Hlakola³, A. Hokwana³, S. W. Hoosen³, D. M. Horn³, J. M. G. Horrell^{3,28}, B. V. Hugo^{3,2}, A. R. Isaacson³, J. L. Jonas^{2,3}, J. D. B. Jordaan^{3,24}, A. F. Joubert³, R. P. M. Julie³, F. B. Kapp³, V. A. Kasper³, J. S. Kenyon^{2,3}, P. P. A. Kotzé³, A. G. Kotze³, N. Kriek³, H. Kriel³, V. K. Krishnan³, T. W. Kusel³, L. S. Legodi³, R. Lehmensiek^{24,26}, D. Liebenberg³, R. T. Lord³, B. M. Lunsy³, K. Madisa³, L. G. Magnus³, J. P. L. Main³, A. Makhaba³, S. Makhathini⁶, J. A. Malan³, J. R. Manley³, S. J. Marais²⁴, M. D. J. Maree³, A. Martens³, T. Mauch³, K. McAlpine³, B. C. Merry³, R. P. Millenaar³, O. J. Mokone³, T. E. Monama²⁹, M. C. Mphego³, W. S. New³, B. Ngcebetsha^{3,2}, K. J. Ngoasheng³, M. T. Ockards³, A. J. Otto^{3,25}, A. A. Patel³, A. Peens-Hough³, S. J. Perkins³, N. M. Ramanujam^{3,30}, Z. R. Ramudzuli³, S. M. Ratcliffe³, R. Renil³, A. Robyntjies³, A. N. Rust³, S. Salie³, N. Sambu³, C. T. G. Schollar³, L. C. Schwardt³, R. L. Schwartz³, M. Serylak^{25,3,19}, R. Siebrits³, S. K. Sirothia^{3,2}, M. Slabber³, L. Sofeya³, B. Taljaard³, C. Tasse^{31,2}, A. J. Tiplady³, O. Toruvanda³, S. N. Twum³, T. J. van Balla³, A. van der Byl³, C. van der Merwe³, C. L. van Dyk³², V. Van Tonder³, R. Van Wyk³, A. J. Venter³, M. Venter³, M. G. Welz³, L. P. Williams³, and B. Xiaia³

(Affiliations can be found after the references)

Received 7 June 2021 / Accepted 25 October 2021

ABSTRACT

MeerKAT's large number (64) of 13.5 m diameter antennas, spanning 8 km with a densely packed 1 km core, create a powerful instrument for wide-area surveys, with high sensitivity over a wide range of angular scales. The MeerKAT Galaxy Cluster Legacy Survey (MGCLS) is a programme of long-track MeerKAT *L*-band (900–1670 MHz) observations of 115 galaxy clusters, observed for ~6–10 h each in full polarisation. The first legacy product data release (DR1), made available with this paper, includes the MeerKAT visibilities, basic image cubes at ~8'' resolution, and enhanced spectral and polarisation image cubes at ~8'' and 15'' resolutions. Typical sensitivities for the full-resolution MGCLS image products range from ~3–5 $\mu\text{Jy beam}^{-1}$. The basic cubes are full-field and span $2^\circ \times 2^\circ$. The enhanced products consist of the inner $1.2^\circ \times 1.2^\circ$ field of view, corrected for the primary beam. The survey is fully sensitive to structures up to ~10' scales, and the wide bandwidth allows spectral and Faraday rotation mapping. Relatively narrow frequency channels (209 kHz) are also used to provide HI mapping in windows of $0 < z < 0.09$ and $0.19 < z < 0.48$. In this paper, we provide an overview of the survey and the DR1 products, including caveats for usage. We present some initial results from the survey, both for their intrinsic scientific value and to highlight the capabilities for further exploration with these data. These include a primary-beam-corrected compact source catalogue of ~626 000 sources for the full survey and an optical and infrared cross-matched catalogue for compact sources in the primary-beam-corrected areas of Abell 209 and Abell S295. We examine dust unbiased star-formation rates as a function of cluster-centric radius in Abell 209, extending out to $3.5 R_{200}$. We find no dependence of the star-formation rate on distance from the cluster centre, and we observe a small excess of the radio-to-100 μm flux ratio towards the centre of Abell 209 that may reflect a ram pressure enhancement in the denser environment. We detect diffuse cluster radio emission in 62 of the surveyed systems and present a catalogue of the 99 diffuse cluster emission structures, of which 56 are new. These include mini-halos, halos, relics, and other diffuse structures for which no suitable characterisation currently exists. We highlight some of the radio galaxies that challenge current paradigms, such as trident-shaped structures, jets that remain well collimated far beyond their bending radius, and filamentary features linked to radio galaxies that likely illuminate magnetic flux tubes in the intracluster medium. We also present early results from the HI analysis of four clusters, which show a wide variety of HI mass distributions that reflect both sensitivity and intrinsic cluster effects, and the serendipitous discovery of a group in the foreground of Abell 3365.

Key words. surveys – galaxies: clusters: general – radio continuum: general – catalogs – radio lines: general – galaxies: general

[★] Data are available at <https://doi.org/10.48479/7epd-w356>.

1. Introduction

Galaxy clusters are the largest gravitationally bound structures in the Universe and, as such, are powerful tools for a variety of research areas in both astrophysics and cosmology. Their composition is dominated by dark matter, with $\sim 13\%$ of their mass coming from the ionised plasma of the intracluster medium (ICM) and only $\sim 2\%$ from the stars of their constituent galaxies and cold gas. Some of these galaxies radiate at radio frequencies, either through star-formation processes or from nuclear activity in the galaxy's core (Condon 1992; Simpson et al. 2006; Luchsinger et al. 2015; Mancuso et al. 2017). Some radio galaxies with active galactic nuclei (AGN) exhibit large-scale radio jets or lobes (Fanaroff & Riley 1974), which can be disrupted by interaction with the ICM through merger-related or other processes (see e.g. Gunn & Gott 1972; Miley et al. 1972; Cowie & McKee 1975; Blanton et al. 2003).

Radio observations of clusters have also revealed steep-spectrum, diffuse radio emission (see reviews by Feretti et al. 2012; van Weeren et al. 2019), which can be used to study the distributed populations of cosmic ray particles and magnetic fields in the ICM, outside of individual radio or star-forming galaxies. These diffuse structures are closely linked to cluster mergers (Cassano et al. 2010; van Weeren et al. 2011a) and as such can also be used to study shock physics, merger-related turbulence, and other particle re-acceleration processes within the ICM (see reviews by Brunetti & Jones 2014; van Weeren et al. 2019, and references therein). Cluster observations carried out by wide-field instruments also contain many field sources, both along the cluster line of sight and in the surrounding area. These provide important information on the clusters themselves (e.g. by using background sources as Faraday rotation probes) and on radio galaxy physics outside of the dense cluster environments. Wide-field imaging enables both statistical studies, such as environment-sensitive properties of galaxy populations, and serendipitous studies of individual field sources (e.g. Brüggén et al. 2021).

MeerKAT¹ is a 64-dish radio interferometer that can observe the sky below a declination (Dec) of $+45^\circ$ (with an elevation limit of 15°), operating in the UHF (580–1015 MHz), *L* (900–1670 MHz), and *S* bands (1.75–3.5 GHz). Its specifications are described in detail in Jonas & MeerKAT Team (2016) and Camilo et al. (2018). MeerKAT's *L*-band system, with a primary beam full width at half maximum (FWHM) of 1.2° at 1.28 GHz, was the first to be commissioned, and in 2018 MeerKAT began a programme of long-track observations of galaxy clusters. This programme became the MeerKAT Galaxy Cluster Legacy Survey (MGCLS), using ~ 1000 h in the *L* band to observe 115 galaxy clusters in full polarisation between -80° and 0° Dec, spread out over the full range of right ascension (RA).

In addition to continuum and polarimetric studies, the deep, broadband, wide-field, sub- $10''$ resolution MGCLS observations provide a rich resource for studying neutral hydrogen in galaxies. Studies of HI morphologies in dense cluster environments and in the field, distributions of HI masses in different types of clusters, and the cosmic evolution of cluster HI out to redshifts of $z = 0.48$ are all enabled with these data, with a velocity resolution of ~ 44 km s⁻¹ at $z = 0$.

Here we present an overview of the MGCLS and the various legacy products being made available to the astronomical community. These data are a rich resource for many scientific

studies, both cluster-specific studies and those involving field sources. We provide some initial science findings in the areas of cluster diffuse emission, radio galaxy physics, star-forming systems, and neutral hydrogen mapping. In addition to their intrinsic value, these examples also demonstrate the potential of the legacy products for a wide range of astrophysical investigations.

The paper is organised as follows. In Sect. 2 we describe the target sample, with the observations and initial data processing described in Sect. 3. A discussion of the legacy data products, including caveats for use and some primary use cases, is provided in Sect. 4. Source catalogues are presented in Sect. 5. The next four sections present highlights of various science investigations that have been or can be carried out using the legacy products and visibilities: Sect. 6 focuses on cluster diffuse emission; Sect. 7 highlights some interesting individual radio sources; Sect. 8 presents results based on star-forming galaxies; and Sect. 9 highlights some HI science capabilities. A summary and concluding remarks are presented in Sect. 10. In this paper we assume a flat Λ cold dark matter cosmology with $H_0 = 70$ km s⁻¹ Mpc⁻¹, $\Omega_m = 0.3$, and $\Omega_\Lambda = 0.7$. We define the radio spectral index, α , such that $S_\nu \propto \nu^\alpha$, where S_ν is the flux density at frequency ν . In this paper R_{200} denotes the radius within which the average density is 200 times the critical density of the Universe. Unless otherwise noted, we give all synthesised beams in terms of FWHM values, and redshifts are taken from the NASA/IPAC right ascension (NED)² (Helou et al. 1991) or Vizier (Ochsenbein et al. 2000).

2. Cluster sample

The MGCLS sample consists of 115 galaxy clusters spanning a Dec range of -85 to 0° . The targeted clusters form a heterogeneous sample, with no mass or redshift selection criteria applied, and consist of two groups: 'radio-selected' and 'X-ray-selected'. The full list of MGCLS clusters is given in Table 1 where the listed RA and Dec are that of the MeerKAT pointing. The median redshift of the sample is 0.14, with only four clusters at $z > 0.4$.

2.1. Radio-selected sub-sample

The radio-selected sub-sample consists of 41 southern targets that have been previously searched for diffuse cluster radio emission by other studies. Targets were selected from published radio studies or reviews, namely Giovannini et al. (1999), Feretti et al. (2012), Lindner et al. (2014), Kale et al. (2015, 2017), Shakouri et al. (2016), Bonafede et al. (2017), George et al. (2017), Giacintucci et al. (2017), Parekh et al. (2017), and Golovich et al. (2019), and include both systems with and without previous diffuse emission detections. These previous radio studies were restricted to high-mass systems, $M_{500} \gtrsim 6 \times 10^{14} M_\odot$, derived from X-ray or Sunyaev-Zel'dovich effect (Sunyaev & Zeldovich 1972) data. Thus, the radio-selected sub-sample contains only high mass clusters. It covers a redshift range of $0.018 < z < 0.87$, with median $z = 0.22$.

Targeting systems of this nature ensured a high scientific return in terms of diffuse emission studies. However, due to the selection, this sub-sample is strongly biased towards clusters with radio halos and relics. The radio-selected clusters are listed

¹ Operated by the South African Radio Astronomy Observatory (SARAO).

² The NASA/IPAC Extragalactic Database is operated by the Jet Propulsion Laboratory, California Institute of Technology, under contract with the National Aeronautics and Space Administration.

Table 1. Observed cluster sample.

| (1) | (2) | (3) | (4) | (5) | (6) | (7) | (8) | (9) | (10) | (11) |
|------------------------------|------------------------------|-------------------------------|----------|-------------------|------|------|--|-----|------|--------------------|
| Cluster name | RA _{J2000} (deg) | Dec _{J2000} (deg) | <i>z</i> | Astrometry Fix | Posn | Pol. | rms (μ Jy beam ⁻¹) | DQF | D.E. | Alternate name |
| <i>Radio-selected sample</i> | | | | | | | | | | |
| Abell 13 | 3.3842 | -19.5010 | 0.094 | - | ✓ | - | 3.5 | 1 | ✓ | MCXC J0013.6-1930 |
| Abell 22 | 5.1608 | -25.7220 | 0.142 | ✓ | ✓ | ✓ | 2.9 | 0 | ✓ | MCXC J0020.7-2542 |
| Abell 33 | 6.7792 | -19.5067 | 0.280 | - | ✓ | - | 5.7 | 1 | - | |
| Abell 85 | 10.4529 | -9.3180 | 0.055 | ✓ | ✓ | ✓ | 3.3 | 1 | ✓ | MCXC J0041.8-0918 |
| Abell 133 | 15.6879 | -21.8800 | 0.057 | ✓ | ✓ | ✓ | 6.7 | 1 | - | MCXC J0102.7-2152 |
| Abell 168 | 18.7908 | 0.2475 | 0.045 | ✓ | ✓ | ✓ | 3.6 | 2 | ✓ | MCXC J0115.2+0019 |
| Abell 194 | 21.4458 | -1.3731 | 0.018 | ✓ | ✓ | ✓ | 5.7 | 1 | - | MCXC J0125.6-0124 |
| Abell 209 | 22.9896 | -13.5764 | 0.206 | ✓ | ✓ | ✓ | 3.6 | 1 | ✓ | MCXC J0131.8-1336 |
| Abell 370 | 39.9604 | -1.5856 | 0.375 | ✓ | ✓ | - | 6.9 | 2 | ✓ | ZwCl 0237.2-0146 |
| Abell 521 | 73.5358 | -10.2442 | 0.253 | - | ✓ | - | 3.4 | 0 | ✓ | MCXC J0454.1-1014 |
| Abell 545 | 83.1017 | -11.5431 | 0.154 | ✓ | ✓ | - | 3.1 | 1 | ✓ | MCXC J0532.3-1131 |
| Abell 548 | 86.7571 | -25.6164 | 0.042 | ✓ | ✓ | ✓ | 2.8 | 1 | - | |
| Abell 2485 | 342.1371 | -16.1064 | 0.247 | - | ✓ | - | 2.8 | 0 | - | MCXC J2248.5-1606 |
| Abell 2597 | 351.3321 | -12.1244 | 0.085 | - | ✓ | - | 6.0 | 2 | - | MCXC J2325.3-1207 |
| Abell 2645 | 355.3200 | -9.0275 | 0.251 | - | ✓ | - | 4.3 | 2 | ✓ | MCXC J2341.2-0901 |
| Abell 2667 | 357.9196 | -26.0836 | 0.230 | - | ✓ | - | 2.7 | 0 | ✓ | MCXC J2351.6-2605 |
| Abell 2744 | 3.5671 | -30.3830 | 0.308 | ✓ | ✓ | ✓ | 2.9 | 0 | ✓ | MCXC J0014.3-3023 |
| Abell 2751 | 4.0580 | -31.3885 | 0.107 | ✓ | ✓ | ✓ | 2.6 | 0 | ✓ | MCXC J0016.3-3121 |
| Abell 2811 | 10.5368 | -28.5358 | 0.108 | - | ✓ | - | 2.6 | 0 | ✓ | MCXC J0042.1-2832 |
| Abell 2813 | 10.8517 | -20.6214 | 0.292 | - | ✓ | - | 3.4 | 2 | ✓ | MCXC J0043.4-2037 |
| Abell 2895 | 19.5463 | -26.9731 | 0.227 | - | ✓ | - | 3.0 | 1 | ✓ | MCXC J0118.1-2658 |
| Abell 3365 | 87.0500 | -21.9350 | 0.093 | - | ✓ | - | 2.8 | 0 | ✓ | |
| Abell 3376 | 90.4256 | -39.9851 | 0.046 | ✓ | ✓ | ✓ | 3.1 | 1 | ✓ | MCXC J0601.7-3959 |
| Abell 3558 | 201.9783 | -31.4922 | 0.048 | ✓ | ✓ | - | 2.9 | 1 | ✓ | MCXC J1327.9-3130 |
| Abell 3562 | 202.7833 | -31.6731 | 0.049 | ✓ | ✓ | ✓ | 3.3 | 0 | ✓ | MCXC J1333.6-3139 |
| Abell 3667 | 303.1403 | -56.8406 | 0.056 | ✓ | ✓ | ✓ | 4.2 | 1 | ✓ | MCXC J2012.5-5649 |
| Abell 4038 | 356.8796 | -28.2028 | 0.028 | ✓ | ✓ | ✓ | 3.0 | 0 | ✓ | MCXC J2347.7-2808 |
| Abell S295 | 41.4000 | -53.0380 | 0.300 | ✓ | ✓ | ✓ | 2.3 | 0 | ✓ | PSZ1 G271.48-56.57 |
| Abell S1063 | 342.1813 | -44.5289 | 0.348 | - | ✓ | - | 2.6 | 0 | ✓ | MCXC J2248.7-4431 |
| Abell S1121 | 351.2844 | -41.2118 | 0.190 | - | ✓ | - | 5.4 | 2 | ✓ | PSZ2 G348.90-67.37 |
| Bullet ^(†) | 104.6579 | -55.9500 | 0.296 | ✓ | ✓ | - | 2.8 | 0 | ✓ | MCXC J0658.5-5556 |
| El Gordo | 15.7188 | -49.2495 | 0.870 | ✓ | ✓ | - | 1.5 | 0 | ✓ | ACT-CL J0102-4915 |
| MACS J0025.4-1222 | 6.3724 | -12.3770 | 0.584 | ✓ | ✓ | - | 3.7 | 1 | - | MCXC J0025.4-1222 |
| MACS J0257.6-2209 | 44.4179 | -22.1628 | 0.322 | - | ✓ | - | 3.2 | 1 | ✓ | MCXC J0257.6-2209 |
| MACS J0417.5-1155 | 64.3942 | -11.9089 | 0.440 | ✓ | ✓ | - | 2.9 | 0 | ✓ | MCXC J0417.5-1154 |
| PLCK G200.9-28.2 | 72.5871 | -2.9493 | 0.220 | ✓ | ✓ | ✓ | 4.4 | 1 | ✓ | |
| RXC J0225.1-2928 | 36.3750 | -29.5000 | 0.060 | ✓ | ✓ | - | 5.1 | 2 | - | MCXC J0225.1-2928 |
| RXC J0510.7-0801 | 77.6846 | -8.0200 | 0.220 | ✓ | ✓ | - | 5.2 | 1 | ✓ | MCXC J0510.7-0801 |
| RXC J0520.7-1328 | 80.1967 | -13.5022 | 0.336 | ✓ | ✓ | - | 7.7 | 2 | ✓ | PSZ1 G215.29-26.09 |
| RXC J1314.4-2515 | 198.5988 | -25.2558 | 0.249 | ✓ | ✓ | - | 4.2 | 1 | ✓ | MCXC J1314.4-2515 |
| RXC J2351.0-1954 | 357.7704 | -19.9133 | 0.248 | - | ✓ | - | 3.1 | 1 | ✓ | |
| <i>X-ray-selected sample</i> | | | | | | | | | | |
| J0014.3-6604 | 3.5767 | -66.0775 | 0.155 | ✓ | ✓ | - | 2.5 | 0 | - | Abell 2746 |
| J0027.3-5015 | 6.8388 | -50.2511 | 0.145 | ✓ | ✓ | - | 2.6 | 0 | ✓ | Abell 2777 |
| J0051.1-4833 | 12.7967 | -48.5597 | 0.187 | ✓ | ✓ | - | 2.6 | 0 | - | Abell 2830 |
| J0108.5-4020 | 17.1383 | -40.3500 | 0.143 | ✓ | ✓ | - | 2.6 | 0 | - | Abell 2874 |
| J0117.8-5455 | 19.4604 | -54.9239 | 0.251 | ✓ | ✓ | - | 2.4 | 0 | - | RXC J0117.8-5455 |
| J0145.0-5300 | 26.2596 | -53.0139 | 0.118 | ✓ | ✓ | - | 2.6 | 1 | ✓ | Abell 2941 |

Notes. Columns: (1) Cluster name, listed alphabetically: Radio-selected targets are indicated by their common name (top panel), X-ray-selected targets are indicated by their MCXC catalogue designation (bottom panel). See Sect. 2 for details; (2) and (3) MeerKAT pointing coordinates: J2000 RA and Dec; (4) Cluster redshift; (5)–(7) Product status: Astrometry (see Sect. 4.4.4) – corrected mapping (Fix) and positional offsets (Posn); Polarisation mapped (Pol.); (8) Image sigma-clipped standard deviation; (9) Data quality flag: 0 – Good dynamic range, 1 – Moderate dynamic range with some artefacts around bright sources, 2 – Poor dynamic range with high contamination by bright source artefacts, 3 – Poor dynamic range with ripples across image; (10) Presence of diffuse cluster emission; see Table 4 for more details; (11) Alternate cluster name. ^(†) Observed as part of the X-ray-selected sample; data products can be found under the MCXC designation, J0658.5-5556.

Table 1. continued.

| (1) Cluster name | (2) RA _{J2000} (deg) | (3) Dec _{J2000} (deg) | (4) z | (5) Astrometry Fix | (6) Pol. Posn | (7) | (8) rms (μ Jy beam ⁻¹) | (9) DQF | (10) D.E. | (11) Alternate name |
|-----------------------------|-------------------------------------|--------------------------------------|----------|--------------------------|---------------------|-----|---|------------|--------------|------------------------|
| J0145.2–6033 | 26.3196 | −60.5650 | 0.184 | ✓ | ✓ | – | 2.3 | 0 | ✓ | PSZ1 G291.34–55.32 |
| J0212.8–4707 | 33.2246 | −47.1328 | 0.115 | ✓ | ✓ | – | 3.1 | 1 | – | Abell 2988 |
| J0216.3–4816 | 34.0796 | −48.2731 | 0.163 | ✓ | ✓ | ✓ | 3.1 | 3 | ✓ | Abell 2998 |
| J0217.2–5244 | 34.3025 | −52.7469 | 0.343 | ✓ | ✓ | – | 2.8 | 1 | ✓ | ACT-CL J0217–5245 |
| J0225.9–4154 | 36.4775 | −41.9097 | 0.220 | ✓ | ✓ | – | 2.7 | 1 | ✓ | Abell 3017 |
| J0232.2–4420 | 38.0700 | −44.3475 | 0.284 | ✓ | ✓ | ✓ | 2.6 | 0 | ✓ | PSZ2 G259.98–63.43 |
| J0303.7–7752 | 45.9433 | −77.8692 | 0.274 | ✓ | ✓ | – | 2.9 | 0 | ✓ | PSZ1 G294.68–37.01 |
| J0314.3–4525 | 48.5825 | −45.4242 | 0.073 | ✓ | ✓ | ✓ | 2.5 | 0 | ✓ | Abell 3104 |
| J0317.9–4414 | 49.4938 | −44.2389 | 0.075 | ✓ | ✓ | – | 3.0 | 2 | – | Abell 3112 |
| J0328.6–5542 | 52.1563 | −55.7128 | 0.086 | ✓ | ✓ | ✓ | 2.9 | 1 | – | Abell 3126 |
| J0336.3–4037 | 54.0779 | −40.6222 | 0.062 | ✓ | ✓ | – | 3.5 | 1 | – | Abell 3140 |
| J0342.8–5338 | 55.7246 | −53.6353 | 0.060 | ✓ | ✓ | – | 3.4 | 0 | ✓ | Abell 3158 |
| J0351.1–8212 | 57.7871 | −82.2167 | 0.061 | ✓ | ✓ | ✓ | 2.8 | 0 | ✓ | Abell S405 |
| J0352.4–7401 | 58.1229 | −74.0308 | 0.127 | ✓ | ✓ | ✓ | 2.6 | 0 | ✓ | Abell 3186 |
| J0406.7–7116 | 61.6908 | −71.2750 | 0.229 | ✓ | ✓ | – | 3.0 | 1 | – | |
| J0416.7–5525 | 64.1871 | −55.4189 | 0.365 | ✓ | ✓ | – | 2.7 | 0 | – | |
| J0431.4–6126 | 67.8504 | −61.4439 | 0.059 | ✓ | ✓ | ✓ | 4.5 | 1 | ✓ | Abell 3266 |
| J0449.9–4440 | 72.4800 | −44.6781 | 0.172 | ✓ | ✓ | – | 2.6 | 0 | – | Abell 3292 |
| J0510.2–4519 | 77.5575 | −45.3211 | 0.200 | ✓ | ✓ | – | 3.0 | 0 | ✓ | Abell 3322 |
| J0516.6–5430 | 79.1583 | −54.5142 | 0.297 | ✓ | ✓ | ✓ | 3.1 | 1 | ✓ | Abell S520 |
| J0525.8–4715 | 81.4650 | −47.2506 | 0.191 | ✓ | ✓ | – | 3.0 | 1 | – | Abell 3343 |
| J0528.9–3927 | 82.2346 | −39.4628 | 0.284 | ✓ | ✓ | – | 2.6 | 0 | ✓ | PSZ2 G244.37–32.15 |
| J0540.1–4050 | 85.0263 | −40.8422 | 0.036 | ✓ | ✓ | – | 4.1 | 1 | – | Abell S540 |
| J0540.1–4322 | 85.0417 | −43.3822 | 0.085 | ✓ | ✓ | ✓ | 3.4 | 1 | – | Abell 3360 |
| J0542.8–4100 | 85.7117 | −41.0014 | 0.640 | ✓ | ✓ | – | 2.4 | 0 | – | CL J0542.8–4100 |
| J0543.4–4430 | 85.8517 | −44.5053 | 0.164 | ✓ | ✓ | – | 3.6 | 1 | – | |
| J0545.5–4756 | 86.3775 | −47.9406 | 0.130 | ✓ | ✓ | – | 2.9 | 1 | – | Abell 3363 |
| J0600.8–5835 | 90.2013 | −58.5872 | 0.037 | ✓ | ✓ | – | 2.5 | 0 | – | Abell S560 |
| J0607.0–4928 | 91.7558 | −49.4833 | 0.056 | ✓ | ✓ | ✓ | 2.8 | 1 | – | Abell 3380 |
| J0610.5–4848 | 92.6333 | −48.8072 | 0.243 | ✓ | ✓ | – | 2.8 | 0 | – | |
| J0616.8–4748 | 94.2233 | −47.8050 | 0.116 | ✓ | ✓ | – | 3.0 | 0 | – | PSZ1 G255.64–25.30 |
| J0625.2–5521 | 96.3179 | −55.3517 | 0.121 | ✓ | ✓ | – | 5.3 | 1 | – | |
| J0626.3–5341 | 96.5950 | −53.6956 | 0.051 | ✓ | ✓ | – | 4.4 | 2 | – | Abell 3391 |
| J0627.2–5428 | 96.8100 | −54.4700 | 0.051 | ✓ | ✓ | ✓ | 7.8 | 2 | ✓ | Abell 3395 |
| J0631.3–5610 | 97.8363 | −56.1722 | 0.054 | ✓ | ✓ | – | 2.7 | 0 | ✓ | |
| J0637.3–4828 | 99.3288 | −48.4783 | 0.203 | ✓ | ✓ | ✓ | 3.0 | 0 | ✓ | Abell 3399 |
| J0638.7–5358 | 99.6938 | −53.9717 | 0.233 | ✓ | ✓ | ✓ | 3.4 | 1 | ✓ | Abell S592 |
| J0645.4–5413 | 101.3721 | −54.2189 | 0.167 | ✓ | ✓ | – | 3.4 | 1 | ✓ | Abell 3404 |
| J0658.5–5556 ^(†) | 104.6296 | −55.9469 | 0.296 | ✓ | ✓ | – | 3.2 | 0 | ✓ | Bullet |
| J0712.0–6030 | 108.0225 | −60.5017 | 0.032 | ✓ | ✓ | – | 2.7 | 1 | – | |
| J0738.1–7506 | 114.5375 | −75.1067 | 0.111 | ✓ | ✓ | – | 2.6 | 0 | – | PSZ1 G287.05–23.21 |
| J0745.1–5404 | 116.2900 | −54.0789 | 0.074 | ✓ | ✓ | ✓ | 3.1 | 0 | ✓ | CIZA J0745.1–5404 |
| J0757.7–5315 | 119.4438 | −53.2636 | 0.043 | ✓ | ✓ | – | 3.2 | 0 | – | Abell S606 |
| J0812.5–5714 | 123.1263 | −57.2350 | 0.062 | ✓ | ✓ | ✓ | 2.9 | 0 | – | PSZ2 G271.60–12.50 |
| J0820.9–5704 | 125.2483 | −57.0797 | 0.061 | ✓ | ✓ | ✓ | 2.9 | 2 | ✓ | PSZ1 G272.08–11.51 |
| J0943.4–7619 | 145.8542 | −76.3325 | 0.199 | ✓ | ✓ | – | 4.4 | 2 | – | CIZA J0943.4–7619 |
| J0948.6–8327 | 147.1642 | −83.4656 | 0.198 | ✓ | ✓ | ✓ | 3.1 | 0 | – | |
| J1040.7–7047 | 160.1867 | −70.7969 | 0.061 | ✓ | ✓ | ✓ | 4.3 | 1 | – | CIZA J1040.7–7047 |
| J1130.0–4213 | 172.5233 | −42.2297 | 0.155 | ✓ | ✓ | – | 2.9 | 1 | ✓ | PSZ1 G287.22+18.13 |
| J1145.6–5420 | 176.4108 | −54.3414 | 0.155 | ✓ | ✓ | – | 3.1 | 1 | – | PSZ1 G293.32+07.33 |
| J1201.0–4623 | 180.2642 | −46.3906 | 0.118 | ✓ | ✓ | – | 3.2 | 0 | – | CIZA J1201.0–4623 |
| J1240.2–4825 | 190.0571 | −48.4328 | 0.152 | ✓ | ✓ | – | 3.3 | 1 | – | |
| J1248.7–4118 | 192.1996 | −41.3078 | 0.011 | ✓ | ✓ | – | 7.1 | 2 | – | Abell 3526 |
| J1358.9–4750 | 209.7371 | −47.8386 | 0.074 | ✓ | ✓ | ✓ | 3.6 | 1 | – | CIZA J1358.9–4750 |
| J1410.4–4246 | 212.6188 | −42.7769 | 0.049 | ✓ | ✓ | – | 3.6 | 1 | – | CIZA J1410.4–4246 |

Table 1. continued.

| (1) | (2) | (3) | (4) | (5) | (6) | (7) | (8) | (9) | (10) | (11) |
|--------------|------------------------------|-------------------------------|-------|-------------------|------|------|-------------------------------------|-----|------|--------------------|
| Cluster name | RA _{J2000} (deg) | Dec _{J2000} (deg) | z | Astrometry Fix | Posn | Pol. | rms ($\mu\text{Jy beam}^{-1}$) | DQF | D.E. | Alternate name |
| J1423.7–5412 | 215.9304 | −54.2033 | 0.300 | ✓ | ✓ | – | 3.5 | 1 | ✓ | CIZA J1423.7–5412 |
| J1518.3–4632 | 229.5950 | −46.5403 | 0.056 | ✓ | ✓ | ✓ | 5.5 | 1 | – | CIZA J1518.3–4632 |
| J1535.1–4658 | 233.7879 | −46.9792 | 0.036 | ✓ | ✓ | – | 4.4 | 3 | – | CIZA J1535.1–4658 |
| J1539.5–8335 | 234.8913 | −83.5922 | 0.073 | ✓ | ✓ | ✓ | 2.7 | 0 | ✓ | |
| J1601.7–7544 | 240.4446 | −75.7461 | 0.153 | ✓ | ✓ | ✓ | 3.7 | 1 | ✓ | PSZ2 G313.88–17.11 |
| J1645.4–7334 | 251.3592 | −73.5817 | 0.069 | ✓ | ✓ | ✓ | 4.8 | 2 | – | PSZ2 G317.58–17.82 |
| J1653.0–5943 | 253.2533 | −59.7331 | 0.048 | ✓ | ✓ | ✓ | 3.6 | 3 | – | PSZ1 G329.36–09.88 |
| J1705.1–8210 | 256.2929 | −82.1739 | 0.074 | ✓ | ✓ | ✓ | 2.8 | 0 | – | Abell 5792 |
| J1840.6–7709 | 280.1550 | −77.1556 | 0.019 | ✓ | ✓ | – | 19.0 | 1 | ✓ | |
| J2023.4–5535 | 305.8500 | −55.5917 | 0.232 | ✓ | ✓ | ✓ | 2.7 | 1 | ✓ | PSZ1 G342.33–34.92 |
| J2104.9–8243 | 316.2446 | −82.7228 | 0.097 | ✓ | ✓ | ✓ | 2.6 | 0 | – | Abell 3728 |
| J2222.2–5235 | 335.5579 | −52.5869 | 0.174 | ✓ | ✓ | – | 4.0 | 1 | – | Abell 3870 |
| J2319.2–6750 | 349.8000 | −67.8400 | 0.029 | ✓ | ✓ | ✓ | 3.5 | 1 | – | Abell 3990 |
| J2340.1–8510 | 355.0429 | −85.1783 | 0.193 | ✓ | ✓ | ✓ | 3.0 | 1 | – | Abell 4023 |

in the first panel of Table 1, using their common names. Where available, an alternate name is provided in the final column of the table. In cases where multiple alternate names exist, the Meta-Catalogue of X-ray-detected Clusters (MCXC; Piffaretti et al. 2011) designation, if available, is given.

2.2. X-ray-selected sub-sample

The X-ray-selected sub-sample, making up 64% of the MGCLS, was selected from the MCXC catalogue, in order to create a sample with no direct prior biases towards or against cluster radio properties. From the list of clusters in the MCXC catalogue that were south of -39° , we selected MGCLS targets as needed to fill gaps in MeerKAT’s observing schedule.

The X-ray-selected clusters, which cover a redshift range of $0.011 < z < 0.640$ with a median of $z = 0.13$, are listed in the second panel of Table 1 using their MCXC catalogue designations. Where relevant, common alternate names are also listed. The X-ray-selected sample covers a luminosity range of $L_X \sim (0.1-30) \times 10^{44} \text{ erg s}^{-1}$, with $\sim 60\%$ of clusters in the range $10^{44}-10^{45} \text{ erg s}^{-1}$.

3. Observations and data reduction

3.1. Observations

The MGCLS observations were carried out between June 24, 2018, and June 16, 2019, using the full MeerKAT array, with a minimum of 59 antennas per observation. The MGCLS clusters were observed using MeerKAT’s L-band receiver (with nominal radio frequency band of 900–1670 MHz) in the 4k correlator mode (4096 channels across the digitised band of 856–1712 MHz) with 8 s integrations.

Data consists of all combinations of the two orthogonal linearly polarised feeds. Each dataset contains observations of the flux density, delay, and bandpass calibrators PKS B1934–638 and/or PMN J0408–6545. These were observed for 10 min every hour with the remaining time cycling between the target cluster (10 min) and a nearby astrometric and phase calibrator (1 min). These observations spanned 8–12 h, cycling between the target cluster and the various calibrator sources, and typically consisted of $\sim 5.5-9.5$ h on source integration, sometimes divided

into multiple sessions. These were scheduled as ‘fillers’ during observing schedule gaps.

3.2. Initial processing

All datasets were calibrated and imaged with a simple procedure, described in Mauch et al. (2020), which also verified the data quality. All calibration and imaging used the OBIT package³ (Cotton 2008).

3.2.1. Calibration and editing

Various processes as described in Mauch et al. (2020) were used to identify data affected by interference and/or equipment failures, which were then edited out, typically resulting in $\sim 50\%$ of the frequency and/or time samples being removed. The remaining data were calibrated in group delay, bandpass, and amplitude and phase. The reference antenna was picked on the basis of the best signal-to-noise ratio (S/N) in the bandpass solutions. Our flux density scale is based on the spectrum of PKS B1934–638 (Reynolds 1994):

$$\log(S) = -30.7667 + 26.4908 \log(\nu) - 7.0977 \log(\nu)^2 + 0.6053 \log(\nu)^3, \quad (1)$$

where S is the flux density in Jy and ν is the frequency in MHz. The uncertainty in the flux-density scale is estimated to be $\sim 5\%$.

Small errors in both time and frequency tagging were discovered after the observations had started and were subsequently corrected. These errors have a small effect on the images, and are more fully described in Sect. 4.4.4. The majority of images were made after the errors were fixed.

3.2.2. Stokes-I imaging

We created the maps using the OBIT wide-band, wide-field imager MFImage. MFImage uses facets to correct for the curvature of the sky, and multiple frequency bins, which are imaged independently and deconvolved jointly, to allow for the antenna

³ <http://www.cv.nrao.edu/~bcotton/Obit.html>

gains and a sky brightness distribution that vary with frequency. A frequency-dependent taper was used to obtain a resolution that remained approximately constant over our $\sim 2:1$ range in frequency. MFImage is described in more detail in Cotton et al. (2018).

The sky within a radius of 0.8° to 1° of the pointing centre was fully imaged, with outlying facets added to cover sources from the Sydney University Molonglo Sky Survey (SUMSS; Bock et al. 1999) 843 MHz catalogue (Mauch et al. 2003) brighter than 5 mJy within 1.5° . Two iterations of phase-only self-calibration, with a 30 s solution interval, were used. Amplitude and phase self-calibration were added if the image contained a pixel with a brightness in excess of 0.3 Jy beam^{-1} . For Stokes- I imaging we used a maximum of 30 000 components, a loop gain of 0.1, and fields were typically CLEANed to a depth of $\sim 50 \mu\text{Jy beam}^{-1}$. No direction-dependent corrections were applied; such corrections may be useful for followup studies of individual fields, but do not affect the science results presented here.

Robust weighting (-1.5 in AIPS/OBIT usage) was used to down-weight the very densely sampled inner portion of the uv -plane. The resulting FWHM resolution was in the range $7.5\text{--}8.0''$. We made images consisting of 14 frequency bins, each with a 5% fractional ($\Delta\nu/\nu$) bandpass. When the imaging was complete, a spectrum was fitted in each pixel of the resulting cube. Off-source noise levels (rms) in images that were not dynamic range limited ranged over $\sim 3\text{--}5 \mu\text{Jy beam}^{-1}$. This is close to the expected thermal noise, with rms confusion expected to be of the order of $1 \mu\text{Jy beam}^{-1}$ (Mauch et al. 2020). The local rms noise varies over the field of view due to contributions from (multiple) strong sources and is a strong function of the target pointing. Primary beam corrections were only applied to the ‘enhanced products’ (see Sect. 4.2).

3.2.3. Reprocessing with polarimetry

Changes from the standard procedure described in Sect. 3.2.1 were needed for polarisation calibration. The MGCLS observations did not contain observations of a polarised calibrator to calibrate the polarisation response of the array. However, each MeerKAT observing session is begun with a calibration using noise signals injected into each antenna that can be used to calibrate the bulk of the phase and delay difference between the two recorded orthogonal linear polarisations. The remainder of the signal path is stable enough that, after this initial calibration, appropriate polarisation calibration is possible using calibration parameters derived from other, properly polarisation-calibrated, data. This procedure is discussed in detail in Plavin et al. (2020); however, we outline the basic steps here for clarity.

Prior to any calibration derived from the data, the initial calibration of the ‘X’ and ‘Y’ linear feeds from the injected noise signals was performed; this removes most of the phase and delay difference between the X and Y systems. The remainder is sufficiently stable that a ‘standard’ calibration using the same reference antenna corrects it. In the parallel hand calibration the two bandpass calibrators, PKS B1934–638 and PMN J0408–6545, are sufficiently weakly polarised that they can be considered unpolarised. After bandpass calibration subsequent gain calibration solved only for Stokes- I terms to avoid disturbing the relative X/Y gain ratio.

Following the parallel-hand calibration, our polarisation calibration procedure was as follows. We required the selected calibration reference antenna to have a set of averaged polarisation calibrations derived from other MeerKAT datasets that had ade-

quate polarisation calibration (including a polarised calibrator). This ‘standard’ set of calibration tables was used to complete the X–Y phase calibration and to correct for on-axis instrumental polarisation via the feed ellipticity and orientation⁴. Since the antennas are equipped with linear feeds, the fundamental reference for the polarisation angle is the nominal orientation of the feeds.

The standard polarisation calibration source 3C286 was used to verify and make final corrections to the polarisation calibration. This source has a polarisation angle of -33° and a rotation measure (RM) equal to zero (Perley & Butler 2013). A correction of several degrees in polarisation angle and about 1 rad m^{-2} in RM is needed to reproduce the assumed polarisation. These corrections are stable over several years and have been applied to all polarisation corrected data.

A selected subset of the clusters were re-calibrated and imaged in MFImage to produce Stokes I , Q , U , and V images; these clusters are indicated in the ‘Poln’ column in Table 1. Due to the lack of internal polarisation calibration, the Stokes V images are not sufficient to detect weakly circular polarised sources, but can work as an overall check of the quality of the calibration. Strongly circularly or linearly polarised sources ($>1\%$) should be easily detectable.

3.2.4. Polarisation imaging

The imaging in full polarisation was similar to the initial imaging in Stokes I (Sect. 3.2.2), but wider and deeper. We used the same 5% frequency bins and the total bandwidth used by the Stokes- I imaging, which allows the recovery of RMs up to $\pm 100 \text{ rad m}^{-2}$ at full sensitivity, with decreasing sensitivity beyond this range. The field of view fully imaged has a radius of 1.2° . In Stokes I , we cleaned to a depth of $\sim 80 \mu\text{Jy beam}^{-1}$, using up to 500 000 components. Stokes Q and U were CLEANed to a depth of $\sim 30 \mu\text{Jy beam}^{-1}$ with up to 50 000 components. Off-source noise values in images that were not dynamic range limited were $\sim 3 \mu\text{Jy beam}^{-1}$.

4. MGCLS data products

The first MGCLS data release (DR1) is made public with this paper⁵, which consists of the MGCLS visibilities, the basic data products (described in Sect. 4.1), and a set of enhanced products (described in Sect. 4.2). All DR1 legacy products are available through a DOI⁶, and the raw visibilities are accessible through the South African Radio Astronomy Observatory (SARAO) Archive Server⁷ with project ID ‘SSV–20180624–FC–01’. We highlight the primary capabilities of the MGCLS data products in Sect. 4.3. (For issues relating to the scientific usability of the various products, see Sect. 4.4).

4.1. Basic products

The basic MGCLS product consists of the standard MFImage output, the structure and description of which are given in Cotton (2019). The basic image product is a cube consisting of 16

⁴ These standard sets of calibration tables are not part of the MGCLS but can be provided upon reasonable request.

⁵ When using DR1 products, this paper should be cited, and the MeerKAT telescope acknowledgement included. See <https://doi.org/10.48479/7epd-w356> for details.

⁶ <https://doi.org/10.48479/7epd-w356>

⁷ <https://archive.sarao.ac.za/>

planes: (1) the brightness at the reference frequency (typically 1.28 GHz, although there are slight variations depending on the observation), from a pixel-by-pixel least-squares fit to the brightness, I , in each frequency channel; (2) the spectral index, α_{908}^{1656} , from the above fit, or a default value of -0.6 , as described below; and (3)–(16) images in frequency channels centred at 908, 952, 996, 1044, 1093, 1145, 1200, 1258, 1318, 1382, 1448, 1482, 1594, and 1656 MHz; the 1200 and 1258 MHz channels are totally blanked for radio frequency interference (RFI).

It should be noted that none of these have primary beam corrections, thus the brightness values and spectral index estimates are biased by the frequency-variable primary beam shape, and are not suitable for quantitative scientific use. These basic products are useful, however, for full-field visual searches and source-finding. Images in Stokes Q , U , and V are provided where available.

4.2. Enhanced products

4.2.1. Primary-beam-corrected image and spectral index cubes

The basic images were corrected for the primary beam at each frequency, as described in [Mauch et al. \(2020\)](#), both at the full resolution of the image, typically $7.5\text{--}8''$, and at a convolved $15''$ resolution to help recover low-surface-brightness features. The primary-beam-corrected images show the inner $1.2^\circ \times 1.2^\circ$ portion of the MGCLS pointing, as primary beam corrections are unreliable beyond this region. Stokes Q , U , and V cubes are provided where available.

The final enhanced image data products are five-plane cubes (referred to as the *5pln* cubes in the following) in which the first plane is the brightness at the reference frequency, and the second is the spectral index, α_{908}^{1656} , both determined by a least-squares fit to $\log(I)$ versus $\log(\nu)$ at each pixel. The third plane is the brightness uncertainty estimate, fourth is the spectral index uncertainty, and fifth is the χ^2 of the least-squares fit. Uncertainty estimates are only the statistical noise component and do not include calibration or other systematic effects. As described in more detail below (see Sect. 4.4.2), a default value of -0.6 is given for the spectral index when the S/N is too low for an accurate fit.

4.2.2. Primary-beam-corrected frequency cubes

We also provide primary-beam-corrected frequency cubes at full and $15''$ resolutions. These cubes consist of the 12 non-blanked frequency planes with centre frequencies as listed in Sect. 4.1. To account for the unreliability of primary beam corrections far from the pointing centre, pixels are blanked as for the *5pln* cubes discussed above. Stokes Q , U , and V cubes are provided when available.

4.3. Primary use cases

The MGCLS legacy products described in Sect. 4 provide powerful datasets for a range of scientific inquiry. Here we highlight the main use cases for the MGCLS data.

4.3.1. Sensitivity to a range of scales

The configuration of the MeerKAT array, with its dense 1 km diameter core of antennas and maximum 7.7 km baseline, allows for exceptional instantaneous sensitivity to a wide range of angular scales. The full-resolution maps have synthesised beam sizes

of $\sim 7.5\text{--}8''$ and rms image noise levels of $\sim 3\text{--}5 \mu\text{Jy beam}^{-1}$, and are sensitive to extended structures up to tens of arcminutes in extent. An example of the central region of one of the MGCLS fields, MCXC J0027.3–5015, is shown in panel A of Fig. 1. The left figure of panel A shows the full-resolution ($7.4'' \times 7.0''$) image, dominated by compact sources with faint extended structure at the centre. To increase the sensitivity to the larger scale structure, the typical procedure is to convolve to a lower resolution. The middle figure shows the convolved $25''$ resolution map of the same patch of sky, which is badly ‘confused’ due to blending of the compact sources, masking the underlying diffuse emission.

To exploit MeerKAT’s sensitivity to large-scale structures, without the problem of source confusion, we filter out all small-scale structure with the technique of [Rudnick \(2002\)](#) using a box size of 19 pixels ($23.75''$), and convolve the resulting ‘diffuse emission’ image to $25''$. Using Fig. 3 in that paper, we can roughly quantify what percentage of the flux will be in the diffuse emission image as a function of the characteristic size of any structure. For a $60''$ structure, $\sim 82\%$ of the flux will be included, with higher percentages for structures of increasing sizes. Smaller scale features will be heavily suppressed, with only 5–10% of the flux remaining at $15''$, and $\sim 0\%$ at $8''$. The result of this process is shown in the right figure of panel A in Fig. 1, where the structure of the diffuse emission is readily visible. The filtered $25''$ resolution or diffuse emission maps referred to in the following sections are made using the above filtering technique. We note that these filtered maps are not included in the legacy products.

4.3.2. In-band spectral index maps

MeerKAT’s wide 0.8 GHz bandwidth in the L band allows for in-band spectral index studies, with primary-beam-corrected spectral index and associated uncertainty maps being part of the legacy products. Panel B of Fig. 1 shows an example spectral index map for a MGCLS radio galaxy with diffuse lobes. As per the caveats discussed in Sect. 4.4.2, a reliable spectral index can only be fit for pixels with $S/N \gtrsim 10$. Spectral index uncertainty maps contain only the statistical uncertainty from the fit, with constrained spectral indices typically having per-pixel statistical uncertainties between 0.05 and 0.2.

4.3.3. Polarisation studies

All of the MGCLS targets were observed in full polarisation, with 44 of the clusters being mapped in polarisation for DR1 (see Table 1 at the end of the paper for the full list). Allowing for the caveats mentioned in Sect. 4.4.5, the sensitivity of the MGCLS polarisation maps will allow for the detection and determination of RMs for a large population of radio sources. Such detections will allow statistical studies of cluster magnetic fields. The determination of RMs of extended sources at high spatial sensitivity will also allow a detailed study of magnetic field strengths and structure across various source morphologies (e.g. radio galaxies and relics). Panel C of Fig. 1 shows an RM map for one such extended source in the Abell 3667 field. This map is discussed in more detail in Sect. 6.1.3.

4.3.4. H I capabilities

In addition to the continuum and polarimetric use cases, the MGCLS visibilities can also be used for H I studies. The MGCLS frequency resolution of 209 kHz corresponds to an H I

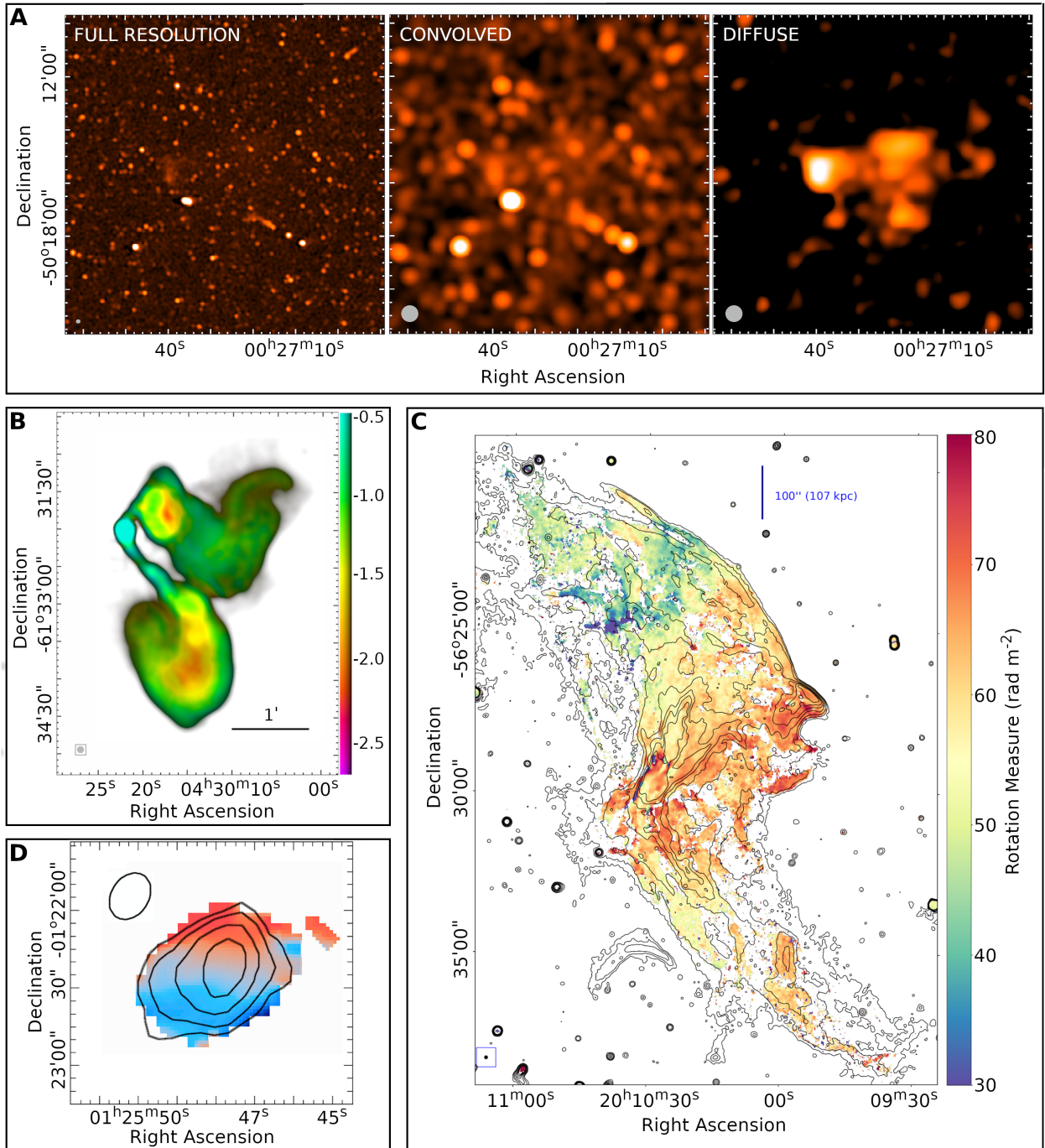


Fig. 1. Capabilities of the MGCLS data. *Panel A:* brightness cutouts from the MCXC J0027.3–5015 field, showing MeerKAT’s instantaneous sensitivity to a range of angular scales. *From left to right:* full-resolution ($7.4'' \times 7.0''$), convolved $25''$ resolution, and filtered ‘diffuse emission’ at $25''$ resolution. The synthesised beam is shown in grey in the lower left corner of each image. The colour scale is in square root scaling in each case, with a minimum and maximum brightness of -10 and $600 \mu\text{Jy beam}^{-1}$ (*left*), 6 and $400 \mu\text{Jy beam}^{-1}$ (*middle*), and 25 and $150 \mu\text{Jy beam}^{-1}$ (*right*), respectively. See Sect. 4.3.1 for further details. *Panel B:* example of an in-band spectral index map of a bent tailed source in the MCXC J0431.4–6126 field, with total intensity coloured by spectral index. The host galaxy, 2MASX J04302197–6132001, is coincident with the radio core (seen in cyan). The colour scale indicates the spectral index, and the brightness gradient of the colour bar indicates intensity, with a burned-out maximum of 10 mJy beam^{-1} . Regions where the S/N was too low to determine a spectral index have been left white. The synthesised beam ($7.1'' \times 6.7''$) is shown by the grey ellipse in the lower left corner. *Panel C:* example of an RM map of a complex MGCLS source in the Abell 3667 field. Contours are Stokes- I intensity with levels of $(5, 10, 20, 40, 60, 80, 100) \times \sigma$, where $\sigma = 6.7 \mu\text{Jy beam}^{-1}$. To avoid including spurious RM values, pixels with Stokes- I intensity below 8σ have been masked. *Panel D:* H I velocity map of Minkowski’s object in Abell 194, at a resolution of $19'' \times 15''$ (beam shown at the top left). Contours show the integrated H I flux density at levels of $(0.35, 0.7, 1.4, 2.5) \text{ mJy beam}^{-1}$. Colours indicate the relative velocity from -22 km s^{-1} (blue) to $+22 \text{ km s}^{-1}$ (red) from the central velocity of 5553 km s^{-1} .

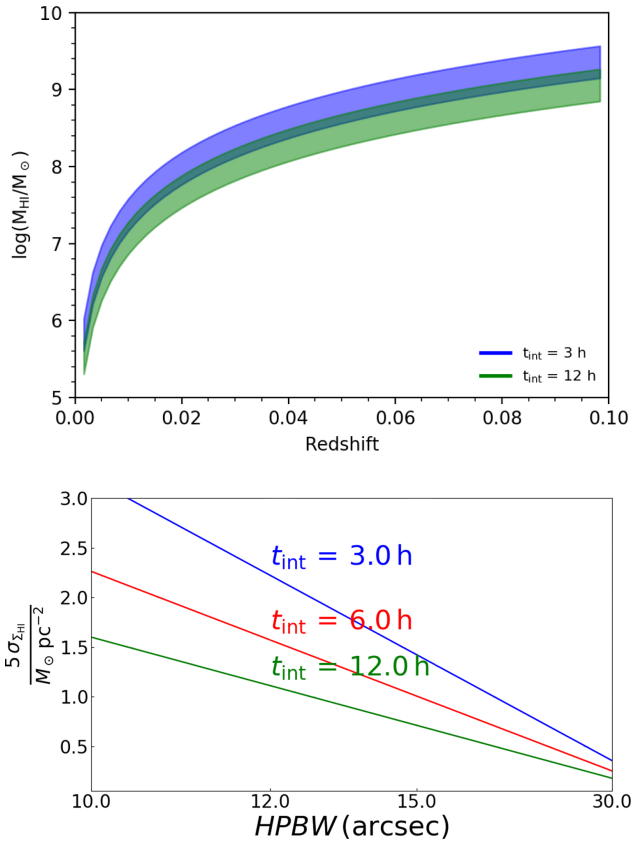


Fig. 2. HI mass sensitivity for the MGCLS. *Top:* logarithm of the total HI mass sensitivity as a function of redshift for integration times between 3 h and 12 h (not all MGCLS datasets have the same usable on-source time for HI analysis). The shaded areas indicate the HI mass limits of the MGCLS data assuming a 5σ detection for a galaxy with line width ranging from 44 km s^{-1} to 300 km s^{-1} . *Bottom:* column-density sensitivity versus angular resolution at $z = 0.03$ for different integration times present in the MGCLS. The horizontal axis scale is proportional to HPBW^{-2} .

velocity resolution of 44.1 km s^{-1} (at $z = 0$). The survey is therefore suitable to approximately resolve the velocity structure of galaxies with a rotational amplitude of $\gtrsim 100 \text{ km s}^{-1}$ (depending on their inclination), which can be seen as a rough threshold dividing dwarf galaxies from more massive objects (Lelli et al. 2014).

The top panel of Fig. 2 shows the HI mass sensitivity as a function of redshift for an integration time of 3 and 12 h (the range of usable on-source time for HI analysis in the MGCLS, with most clusters having 6–10 h on-source), demonstrating that the MGCLS observations are able to detect galaxies below the ‘knee’ of the HI mass function ($\log(M_{\text{HI}}^*/M_{\odot}) = 9.94$, Jones et al. 2018) out to $z \lesssim 0.1$. Moreover, the angular resolution provided by the survey, shown in the bottom panel of Fig. 2, enables one to resolve the structure of the HI in galaxies with a resolution between $10''$ and $30''$, corresponding to a spatial resolution of ~ 4 – 20 kpc at redshifts of $0.02 < z < 0.1$. This means that for clusters in this range, larger galaxies will be spatially resolved and we can conduct studies of resolved HI galaxies while simultaneously probing extended extragalactic structures in the wide field of view – a key discriminating feature with respect to single-dish HI surveys of rich environments. Panel D in Fig. 1 shows an example of a resolved HI detection, covering

two consecutive channels, in the Abell 194 field. Examples of HI science from the MGCLS datasets are given in Sect. 9.

4.4. Data quality issues

There are a number of issues with data quality in the DR1 release that affect the visibilities and images. The images have been corrected for a number of these effects, as described below. However, they still affect the visibilities, and impose limitations on the accuracy of the images. Users of the data products should take these into consideration when scientific analyses are performed.

4.4.1. Dynamic range

Fields with very strong sources ($I > \text{few } 100 \text{ mJy beam}^{-1}$) are typically limited by residual artefacts from the brighter sources. This is especially true if there are several widely separated bright sources, as the self-calibration cannot correct direction-dependent effects (DDEs). The DDEs that are thought to dominate are asymmetries in the antenna pattern, pointing errors, and ionospheric refraction.

4.4.2. Flux density and spectral index

Uncertainties in the primary beam pattern affect both the derived brightnesses and spectral indices. Near the centre of each field, the total array pattern is very close to that of the individual antennas (Mauch et al. 2020). However, application of this individual antenna pattern to spectra of sources in the outer parts of cluster fields produces non-physical results. This is expected because the array power pattern is broadened by pointing errors in the individual antennas. Derived brightnesses, and especially spectral indices, are therefore not reliable beyond a radius of $36'$.

We compared the flux densities of the MGCLS compact sources with those from other radio surveys, as discussed in Sect. 5.2.1, and found them to agree to within about 6%, with the MeerKAT flux densities being, on average, $6\% \pm 4\%$ lower than those of the other two catalogues. No corrections to the flux densities have been made in either the catalogues or the maps.

While MeerKAT’s very wide fractional bandwidth improves the sensitivity and gives us the ability to derive in-band spectral indices, it also creates uncertainties regarding the effective central frequency at each pixel. Simple averaging in frequency space would result in effective reference frequencies that depend on the spectra of the sources in question and their position in the field. When we can adequately fit the spectrum, typically requiring a $S/N \geq 10$, the brightness is calculated correctly at the well-defined reference frequency of 1.28 GHz. The spectral fit was accepted if the χ^2 per degree of freedom was less than 1.5 times the χ^2 per degree of freedom based on assuming the default value of -0.6 ; otherwise the default value is reported and the central frequency brightness is calculated with that spectral assumption. This results in an underestimate of the brightness by $\sim 6\%$ (10%) for a true spectral index of -1 (-2). Typically, these are less than the random errors in these low brightness cases.

Since the flux density threshold for switching to the default spectral index depends on the local noise properties of each cluster image, no global value can be specified. However, inspection of the spectral indices as a function of flux density for a selected region reveals the appropriate local threshold below which the default spectral index has been assigned. Caution is still advised when examining regions of maps where spectral indices very close to the default value are encountered.

4.4.3. Largest angular size

MeerKAT has very good short baseline coverage, allowing recovery of extended emission. However, the minimum baseline length of 29 m does restrict the maximum size of a structure that is properly imaged. This maximum size scales inversely with frequency. Angular scales of less than $10'$ should be fully recovered. Larger scales are less well imaged, especially at the higher frequencies. This effect leads to negative holes around bright extended structures and an artificial apparent steepening of the spectrum. Very steep fitted spectra of extended emission should be treated with caution.

4.4.4. Astrometry

A number of instrumental issues can affect the accuracy of the astrometry. As detailed in this section, we correct the image astrometry in each field by matching the positions with those of the respective optical hosts. This results in a final accuracy better than $0.3''$ in the high S/N limit. However, the astrometric errors are still present in the visibility data, and users that reprocess raw data need to take these into consideration.

Data in the earliest observations suffered from a 2-second time offset in the labelling of the data, and a half-channel frequency error, which propagate into errors in the u, v, w coordinates. The column 'Fix' in Table 1 indicates cluster fields where this issue was corrected in the visibilities. Fields that were not fixed will contain rotation and scaling errors in the positions of sources that depend on position in the field. These can be as large as $2''$ at the edge of the fields.

Calibrator position errors were present in the initial MeerKAT calibrator list, affecting several calibrators up to a level of several arcseconds. This results in an approximately constant position offset of sources in the affected cluster fields. Corrections were made in the images when incorrect calibrator positions were discovered, but the final corrections were made at the end, in any case, through optical cross-matching.

A low-accuracy delay model in the correlator in use during the observations can cause a similar, albeit subtler, problem when the calibrator and target are widely separated. An additional bias is possible when the calibrator does not sufficiently dominate the visibility intensities in the field. The model had insufficient accuracy to reliably transfer phases measured on the calibrator to those of the target, especially since many of the astrometric calibrators were 10° or more from the target. This resulted in approximately constant position offsets of up to several arcseconds in individual fields, which had to be corrected.

Astrometric corrections were made for each field centre, removing or reducing the effects noted above. We matched compact radio components to a large number of background quasars, radio galaxies, and star-forming galaxies in each field, using the optical and infrared catalogues from the Dark Energy Camera Legacy Survey (DECaLS; Dey et al. 2019). A flux density-weighted average correction was determined for every cluster field, as indicated in column 'Posn' in Table 1, and appropriate corrections made to each corresponding image. Residual systematic errors should be under $0.1''$ for clusters as a whole, although errors may be larger for individual sources.

Additional astrometric checks were carried out after the above correction by cross-matching with sources from the International Celestial Reference Frame (ICRF) catalogue (Charlot et al. 2020). Since the ICRF constitutes the most accurately known set of astronomical positions, they are an ideal check of the astrometry in the MGCLS catalogue described

in Sect. 5.2. There are eight ICRF sources in our cluster fields. They are bright (0.3 to 1.8 Jy), and the statistical uncertainty in their MeerKAT position determinations are therefore small. They were chosen for the ICRF for being compact on milliarcsecond scales, and they generally do not have structure on the MeerKAT's $\sim 8''$ scale, which might affect the position determination. We therefore compared our catalogue positions with the ICRF3⁸ ones for the eight sources that were included in our fields: ICRF J010645.1–403419, J025612.8–213729, J031757.6–441417, J033413.6–400825, J060031.4–393702, J062552.2–543850, J124557.6–412845, and J133019.0–312259.

We found that most of the MGCLS catalogue positions differed from the ICRF3 ones by less than $1''$ in either coordinate. The single exception was ICRF J025612.8–213729 (QSO B0253–218) for which the MGCLS catalogue position was $\sim 2.3''$ north of the ICRF3 position. This source is an exception to the above generalisation about lack of structure, in that Reid et al. (1999) show it to be somewhat extended in a N–S direction at 5 GHz, with several components spread out over $\sim 10''$. This field, MACS J0257.6–2209, is also one of the few for which there were uncorrected timing and frequency errors (Col. 5 in Table 1, discussed earlier in this section) that will cause position errors far from the field centre. In addition, since the source is resolved, the MGCLS position at 1.28 GHz and $\sim 8''$ resolution could differ from the ICRF3 position, which is that of the milliarcsecond core only at 5 GHz.

Ignoring this source, we find that for the remaining seven sources the difference between the MGCLS catalogue positions and the ICRF3 ones were $-0.04 \pm 0.34''$ in RA and $-0.02 \pm 0.15''$ in Dec. This check gives us confidence that the positions in the MGCLS catalogue are accurate, and adopt the uncertainty of $0.36''$ based on the ICRF3 comparisons.

4.4.5. Polarisation

The first plane of the Stokes Q and U $5pln$ cubes (see Sect. 4.2.1) provide a good indication of where significant polarisation is present, but should not be used quantitatively on their own. Each image was created by a noise-weighted sum of the frequency planes in the full cube, which is strictly correct only when both the RM and the spectral index are zero, and when no depolarisation is present. At any $RM \neq 0$, the amplitude of Q and U will be reduced, reaching a factor of 2 reduction at $|RM| \sim 25 \text{ rad m}^{-2}$, depending on the source spectral index and the noise in the different frequency channels. The first plane of the Stokes Q and U $5pln$ cubes should therefore be used quantitatively with caution.

We note that polarisation leakage affects the upper half of the band, with the residual polarisation leakage increasing with distance from the field centre within the half-power region of the beam (de Villiers & Cotton, priv. comm.; de Villiers et al. 2021). The instrumental polarisation may reach up to 10% in the upper part of the band, while it is typically less than 2% at the lower frequencies. Users should evaluate how the leakage affects their particular science case.

5. MGCLS source catalogues

We produced source catalogues for all fields in the MGCLS, based on the intensity plane of the full-resolution enhanced products described in Sect. 4.2. Here we detail our source finding

⁸ <http://hpiers.obspm.fr/icrs-pc/newwww/icrf/index.php>

method, as well as the various catalogues being provided with the legacy data products. Limitations to the accuracy of the results are discussed in Sect. 4.4. It is very important to note that these catalogues are not complete, and any statistical analyses must consider their limitations. In particular, the sensitivity depends on the distance from the respective field centres, and regions around bright sources are excluded, as discussed below.

5.1. Source detection

We used the Python Blob Detection and Source Finder (PYBDSF; Mohan & Rafferty 2015) software to create individual source catalogues for all MGCLS fields, using the full-resolution, primary-beam-corrected data products. PYBDSF searches for islands of emission and attempts to fit models consisting of one or more elliptical Gaussians to them. Gaussians are then grouped into sources, and there may be more than one source per island. Each source is given a code: ‘S’ for single-Gaussian sources that are the only source on its island, ‘C’ for single-Gaussian sources that share an island with other sources, and ‘M’ for sources composed of two or more Gaussian fits. We used the default $3\sigma_{\text{img}}$ island boundary threshold and $5\sigma_{\text{img}}$ source detection threshold, where σ_{img} is the local image rms. As many images have variable image noise levels across the field, we allow PYBDSF to calculate the 2D rms map during the source finding.

For sources in regions of high image noise, for example those near bright sources with strong sidelobes, the typical statistical uncertainty in peak source brightness is a factor of ~ 2 larger than for sources elsewhere in the same field. Spurious source detections are common around very bright sources, with PYBDSF sometimes cataloguing sidelobes as sources. To mitigate spurious detections in our DR1 catalogues, we excised all catalogue entries around bright sources. A source was considered bright if its peak brightness was higher than the bright source limit for that field, $I_{\text{lim}}^{\text{bs}}$. This limit is connected to the image dynamic range, such that

$$I_{\text{lim}}^{\text{bs}} = 10^{-4} \times \frac{I_{\text{max}}}{\sqrt{\sigma_{\text{global}}}} \text{ Jy beam}^{-1}, \quad (2)$$

where I_{max} is the maximum source brightness in the image, and σ_{global} is the median image rms, both in units of Jy beam^{-1} . The region around a bright source within which catalogue entries were excised, r_{cut} , scales with the source brightness:

$$r_{\text{cut}} = 0.005 \times \left(1 + \log_2 \frac{I_{\text{peak}}^{\text{bs}}}{I_{\text{lim}}^{\text{bs}}} \right) \text{ deg}, \quad (3)$$

where both $I_{\text{lim}}^{\text{bs}}$ and $I_{\text{peak}}^{\text{bs}}$, the peak brightness of the bright source, are in Jy beam^{-1} . A median of 2.6% of nominally detected sources were removed per field through this process.

5.2. Compact source catalogue

From our PYBDSF results, we compiled a single MGCLS compact source catalogue from all fields, only including sources that could be fit with a single Gaussian component (source codes ‘S’ or ‘C’), after the spurious source excision. The full DR1 catalogue⁹ contains $\sim 626\,000$ sources from the 115 cluster fields, with an excerpt shown in Table 2. The catalogue columns, described in the Table caption, contain standard radio source information including the integrated flux density, peak brightness, and source size, with catalogue source

positions provided in decimal degrees. The source identifier (first column of the catalogue) uses an International Astronomical Union (IAU) classification, with the designation MKTCS JHHMMSS.ss±DDMMSS.s, where the decimal positional information is truncated, rather than rounded.

5.2.1. Comparison with previous radio catalogues

To verify the MGCLS compact source flux densities, we compare them to those from other radio surveys. To cover all MGCLS pointings, we use catalogues from both the 1.4 GHz NRAO VLA Sky Survey (NVSS; north of -40° Dec; Condon et al. 1998) and the 843 MHz SUMSS survey (south of -30° Dec; Bock et al. 1999). To scale the NVSS and SUMSS flux densities to the MGCLS reference frequency of 1.28 GHz, we assume a power law $S_\nu \propto \nu^\alpha$ with a fiducial spectral index of $\alpha = -0.7$ (Smolčić et al. 2017).

To avoid incompleteness effects due to differences in sensitivity between the three surveys, we consider only sources with $S/N \geq 50$ in all three surveys. This high limit also minimises effects from additional faint MGCLS sources within the larger NVSS and SUMSS beams, as noted below. To cross-match MGCLS compact sources with their NVSS and SUMSS counterparts, we use a $5''$ radius. This radius is a compromise between maximising the number of real counterparts and minimising the number of spurious matches. By shifting the MGCLS sources by $1'$ and repeating the cross-matching, we determine that the expected percentage of spurious matches is 4.1% and 3.8% for NVSS and SUMSS, respectively. These have a negligible effect on the flux density comparisons.

Our cross-matching yields a total of 398 and 565 compact MGCLS sources with NVSS and SUMSS counterparts, respectively. Figure 3 shows the flux density scale comparison between the MGCLS compact sources and the scaled NVSS (top panel) and scaled SUMSS (bottom panel) sources. The MGCLS flux densities are in good agreement with those of both NVSS and SUMSS. We fit a power law of the form

$$S_{\text{scaled_cat}} = \kappa \times S_{\text{MGCLS}}^\gamma \quad (4)$$

to the MGCLS and scaled NVSS and SUMSS flux densities. Values of 1 for both κ and γ would indicate an exact one-to-one correspondence. We obtain fit values of $\kappa_{\text{NVSS}} = 1.06 \pm 0.02$, $\gamma_{\text{NVSS}} = 1.00 \pm 0.01$, and $\kappa_{\text{SUMSS}} = 1.06 \pm 0.04$, $\gamma_{\text{SUMSS}} = 1.00 \pm 0.01$ for the NVSS and SUMSS comparisons, respectively. This is consistent with a linear relation between the MGCLS and scaled fluxes, with the scaled NVSS and SUMSS fluxes being marginally higher than those from MGCLS. The MGCLS sources were not chosen to be isolated, so the poorer resolution of the sky surveys ($\sim 45''$) may lead to a single NVSS or SUMSS source having contributions from additional faint MGCLS sources; at the lowest fluxes, this could result in a small bias in opposite spectral index directions for the two surveys. However, the equality of the fitted flux densities show that any such effects are negligible.

We also examine the spectral index distribution of the radio cross-matched MGCLS compact sources. For this purpose, we include 148 MHz data from the TIFR GMRT Sky Survey (TGSS; north of -53° Dec; Intema et al. 2017) in addition to the NVSS and SUMSS surveys. Given the different sky coverages, some MGCLS sources have flux densities at only one additional frequency, whereas others have three. We fit a single $S_\nu \propto \nu^\alpha$ power-law and inspected each fit to discard both spurious matches and sources showing spectral curvature. Figure 4 shows the resulting spectral index distributions. The distributions of

⁹ Available at <https://doi.org/10.48479/7epd-w356>

Table 2. Excerpt of the MGCLS compact source catalogue at 1.28 GHz.

| (1) | (2) | (3) | (4) | (5) | (6) | (7) | (8) | (9) | (10) | (11) | (12) | (13) |
|---------------------|---------------------|----------------------|--------|--------|-----------------------------------|-------------------------|------------------------------------|--------------------------|------------------|------------------|-------------------|----------|
| Src. name | RA _{J2000} | Dec _{J2000} | ΔRA | ΔDec | $S_{\text{tot}}^{1.28\text{GHz}}$ | ΔS_{tot} | $I_{\text{peak}}^{1.28\text{GHz}}$ | ΔI_{peak} | s_{max} | s_{min} | $s_{\text{p.a.}}$ | Field |
| MKTCS | (deg) | (deg) | (deg) | (deg) | (mJy) | (mJy) | (mJy b ⁻¹) | (mJy b ⁻¹) | ($''$) | ($''$) | ($^{\circ}$) | |
| J001059.77–190940.3 | 2.7491 | −19.1612 | 0.0000 | 0.0000 | 0.695 | 0.020 | 0.669 | 0.011 | 7.6 | 7.5 | 6 | Abell_13 |
| J001059.94–190654.9 | 2.7498 | −19.1153 | 0.0001 | 0.0002 | 0.113 | 0.028 | 0.081 | 0.013 | 9.8 | 7.8 | 21 | Abell_13 |
| J001059.14–195204.2 | 2.7464 | −19.8679 | 0.0002 | 0.0003 | 0.106 | 0.027 | 0.056 | 0.010 | 14.2 | 7.3 | 143 | Abell_13 |
| J001059.23–194540.7 | 2.7468 | −19.7613 | 0.0002 | 0.0003 | 0.077 | 0.024 | 0.045 | 0.010 | 11.1 | 8.4 | 153 | Abell_13 |
| J001059.50–192405.3 | 2.7479 | −19.4015 | 0.0001 | 0.0001 | 0.050 | 0.012 | 0.060 | 0.007 | 8.0 | 5.8 | 179 | Abell_13 |
| J002318.34–254121.6 | 5.8264 | −25.6894 | 0.0001 | 0.0002 | 0.053 | 0.016 | 0.061 | 0.010 | 7.4 | 6.5 | 10 | Abell_22 |
| J002317.08–253627.2 | 5.8212 | −25.6076 | 0.0000 | 0.0000 | 0.939 | 0.021 | 0.827 | 0.011 | 8.3 | 7.6 | 36 | Abell_22 |
| J002318.08–253621.5 | 5.8253 | −25.6060 | 0.0002 | 0.0001 | 0.073 | 0.021 | 0.067 | 0.011 | 8.5 | 7.1 | 62 | Abell_22 |
| J002317.47–252111.6 | 5.8228 | −25.3532 | 0.0001 | 0.0001 | 0.242 | 0.030 | 0.198 | 0.015 | 8.6 | 7.8 | 143 | Abell_22 |
| J002317.15–261532.9 | 5.8215 | −26.2592 | 0.0003 | 0.0001 | 0.573 | 0.095 | 0.156 | 0.021 | 19.6 | 10.3 | 80 | Abell_22 |

Notes. The full catalogue, which includes all cluster fields, is available online at <https://doi.org/10.48479/7epd-w356>. Columns: (1) MGCLS source ID using the IAU designation of the form MKTCS JHHMMSS.ss±DDMMSS.s, where the decimals are truncated; (2)–(5) J2000 RA and Dec, and associated 1σ uncertainty, respectively; (6) and (7) Total integrated Stokes- I flux density and associated 1σ uncertainty at the reference frequency, respectively; (8) and (9) Peak Stokes- I brightness and associated 1σ uncertainty, respectively; (10) and (12) Source size: FWHM of the major and minor axes of the source, and source p.a.; (13) Cluster field of the source. All uncertainties are statistical only and are determined from the images as per Condon (1997).

spectral indices for sources with two, three, and four frequency points are similar, although the $N_{\nu} = 4$ distribution has a lower median spectral index. Subtle differences may reflect differences in the spectral populations of the different surveys, but are beyond the scope of the current work.

5.2.2. Optical cross-matching

We created optical cross-match catalogues for the compact sources in the Abell 209 and Abell S295 fields using data from DECaLS (Dey et al. 2019). These fields were selected due to their existing DECaLS coverage and their decent MGCLS dynamic range. Cross-match catalogues for other MGCLS fields will be compiled in follow-up works.

To identify DECaLS counterparts for the MGCLS compact sources, we used the likelihood ratio (LR) method (Sutherland & Saunders 1992; Laird et al. 2009; Smith et al. 2011). The LR here is defined as the ratio of the probability that an optical source (at a given distance from the radio position and with a given optical magnitude) is the true counterpart, to the probability that the same source is a spurious alignment, that is, $\text{LR} = (q(m) \times f(r))/n(m)$, where $q(m)$ is the expected number of true optical counterparts with magnitude m , $f(r)$ is the probability distribution function of the positional uncertainties in both the radio and the optical source catalogues, and $n(m)$ is the background density of optical galaxies of magnitude m in the DECaLS r band (or g or z band). The magnitudes are AB magnitudes from DECaLS DR8.

The a priori probability $q(m)$ is determined as follows. First, the radio and optical source catalogues are matched by finding the closest counterpart within a fixed search radius of $4''$. We chose this radius based on our distributions of cross-matches, as shown in Fig. 5, where the distributions ($\text{LR} > 0.5$) of the RA and Dec angular separations between the positions of radio sources can be approximated by Gaussians. The search radius of $4''$ is the optimal radius where we detect the most true sources. Radii greater than $4''$ will sharply increase the number of spurious matches. The number of spurious matches (of magnitude m) is estimated by scaling $n(m)$ to the area of $4''$ radius within which we search for counterparts. This is then subtracted from the number of counterparts (as a func-

tion of magnitude) to determine the number of true associations, $q(m)$.

In our case, the probability distribution $f(r)$ is a two-dimensional Gaussian distribution:

$$f(r) = \frac{1}{2\pi\delta^2} \exp\left(-\frac{r^2}{2\delta^2}\right). \quad (5)$$

Here, r is the angular distance (in arcsec) from the radio source position, and δ is the combined positional error given by $\sqrt{\delta_{\text{decals}}^2 + \delta_{\text{mgcls}}^2}$, where δ_{decals} is the positional uncertainty from the DECaLS catalogue, and δ_{mgcls} is the positional uncertainty from the MGCLS compact source catalogue. For each source in the MGCLS DR1 compact source catalogue, we adopted an elliptical Gaussian distribution for the positional errors, with the uncertainties in RA and Dec on the radio position reported in the radio catalogue. We assume a systematic optical position uncertainty of $0.2''$ in both RA and Dec for the DECaLS catalogue (Dey et al. 2019).

The optical cross-match catalogue includes all matches within $4''$ of a compact MGCLS source detection, along with their LR probabilities and flags (no LR cutoff imposed). Table 3 shows an excerpt from the optical cross-match catalogue for the Abell 209 field, with the full catalogues for it and the Abell S295 fields available online¹⁰. The presence of more than one counterpart for a particular radio source provides additional information to that contained in the LR itself, which can then be used to estimate the reliability of the counterpart source, or the probability that a particular source is the correct counterpart. The reliability for radio source i , as defined by Sutherland & Saunders (1992), is calculated as

$$\text{REL}_i = \frac{\text{LR}_i}{\sum \text{LR}_{\text{search radius}} + (1 - Q)}, \quad (6)$$

where $\sum \text{LR}_{\text{search radius}}$ is the sum of LR for all possible DECaLS counterparts to the radio source within our search radius of $4''$, and Q is the fraction of MGCLS compact radio sources with optical counterparts above the DECaLS magnitude limit. Comparison of $\sum \text{REL}_i$ with the total number of counterparts with

¹⁰ <https://doi.org/10.48479/7epd-w356>

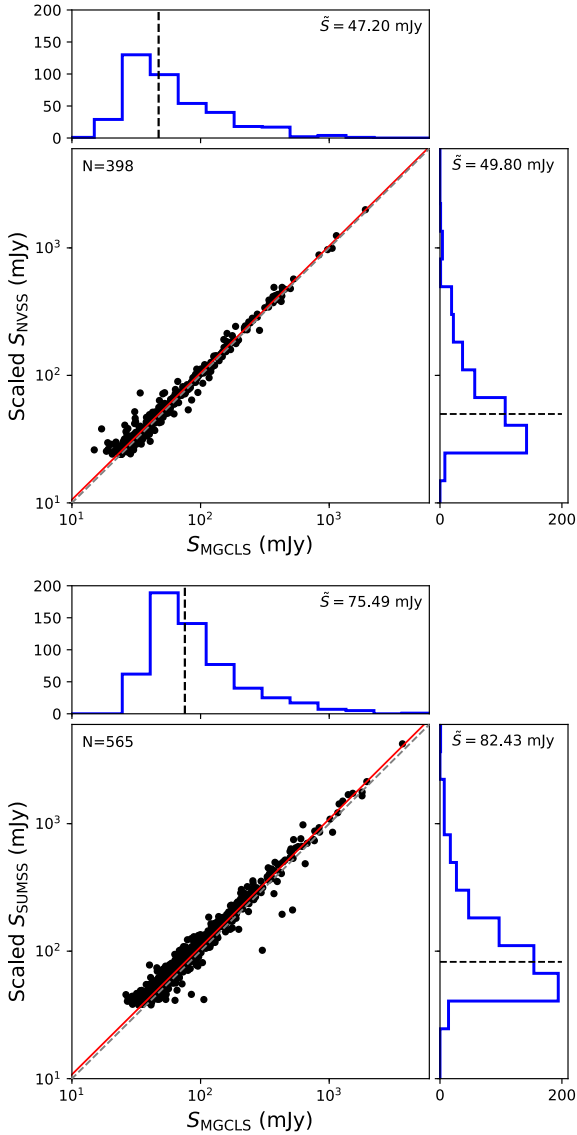


Fig. 3. Comparison between the integrated flux density of MGCLS compact sources with their counterparts in the NVSS (*top*) and SUMSS (*bottom*) catalogues, with the latter two being scaled to the MGCLS frequency of 1.28 GHz. The best-fit relation in each case is shown by the solid red line and is consistent with a linear relationship, with the number of sources in the fit shown in the upper left corner. The dashed grey line shows the exact one-to-one relationship. The scaled sky survey flux densities are typically 6% higher than their MGCLS counterparts, so this represents a possible small bias in the MGCLS flux scale. Histograms show the relevant flux density distributions, with the dashed black lines indicating the respective median values, \tilde{S} .

$LR > LR_{\text{cutoff}}$ provides an estimate of the spurious identification rate, or error rate (ER). The choice of the cutoff in LR is a trade-off between maximum completeness and maximum purity. Completeness is defined as the fraction of radio catalogue sources that have an optical counterpart, and purity (given by $1 - ER$) is the fraction of radio-optical source matches that are real.

Figure 6 shows the completeness and purity for both Abell 209 and Abell S295, with no LR cutoff imposed. Our chosen LR_{cutoff} of 0.5 is indicated by the vertical dotted line. A value of $LR_{\text{cutoff}} = 0.5$ corresponds to an estimated spurious identification rate of 4.5% in Abell 209, with 59% (2723 of 4581) of

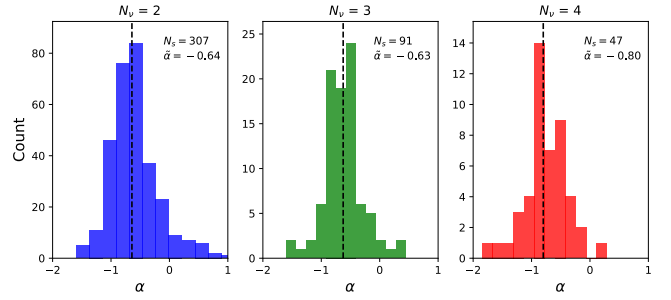


Fig. 4. Spectral index distributions for the cross-matched MGCLS compact sources, using data from the MGCLS (1.28 GHz), NVSS (1.4 GHz), SUMSS (843 MHz), and TGSS (148 MHz) catalogues. *Left to right*: distributions for MGCLS sources with flux density measurements at two, three, and four frequencies, respectively. The number of compact sources, N_s , and the median spectral index, $\tilde{\alpha}$, are indicated in the upper right corner of each panel, and the respective median spectral indices are indicated by vertical dashed lines.

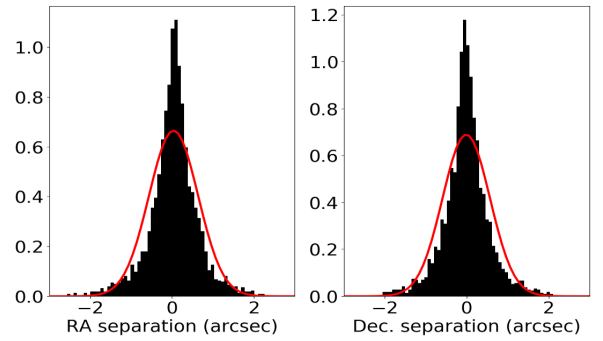


Fig. 5. Histograms of the RA and Dec angular separations between the positions of radio sources in the Abell 209 compact source catalogue and their optical counterparts, for $LR > 0.5$. In each panel, the red line shows the normalised Gaussian distribution.

radio sources in the Abell 209 compact source catalogue having optical counterparts.

5.3. Extended sources

We do not provide catalogues for the extended sources, that is, those for which the PYBDSF fit required multiple Gaussians, indicated in the PYBDSF output with code ‘M’. These need to be verified visually, a process that is extremely time consuming. However, to provide an indication of the number of extended sources in the MGCLS, we performed this verification for sources in the Abell 209 and Abell S295 fields.

Extended sources can be separated into two categories: blended sources (i.e. those with overlapping Gaussian components) and multi-component sources with multiple, non-overlapping, and often visually separable components. There are 158 and 347 blended sources in the Abell 209 and Abell S295 fields, respectively, roughly 3–5% of the number of compact sources in the respective fields. Their integrated flux densities range from $85 \mu\text{Jy}$ to 105 mJy, with the largest blended sources being just over $30''$ across. Extrapolating these numbers to the full MGCLS sample, there are of the order of 29 000 blended sources in the full survey.

We defined the multi-component sources as those with distinct structures such as jets, cores, or lobes. Identifying the different components that comprise a single source can be difficult,

Table 3. Excerpt of the compact source catalogue for Abell 209 with optical cross-match information from DECaLS.

| (1) | (2)–(11) | (12) | (13) | (14) | (15) | (16) | (17) | (18) | (19) | (20) | (21) | (22) | (23) | (24) | (25) | (26) | (27) | (28) |
|---------------------|----------|-------------------|--------------------|----------|----------|----------|--------|--------|-----------------------|------------|------------|------------|-------------|-------------|----------|------------------------|----------------------------|-----------------------------|
| Src. name | | RA _{opt} | Dec _{opt} | <i>g</i> | <i>r</i> | <i>z</i> | W1 | W2 | <i>z</i> _p | Δg | Δr | Δz | $\Delta W1$ | $\Delta W2$ | <i>d</i> | <i>F</i> _{xm} | <i>P</i> _{has_xm} | <i>P</i> _{this_xm} |
| MKTCS | | (deg) | (deg) | | | | | | | | | | | | ($''$) | | | |
| J231022.80–140627.7 | ... | 23.17312 | −14.10746 | 19.469 | 19.01 | 18.772 | 19.115 | 19.448 | 0.22 | 0.003 | 0.003 | 0.008 | 0.03 | 0.095 | 1.1 | 1 | 1 | 1 |
| J231014.16–135358.5 | ... | 23.17047 | −13.89944 | 21.503 | 20.748 | 20.244 | – | – | 0.25 | 0.008 | 0.005 | 0.01 | – | – | 0.8 | 1 | 1 | 1 |
| J231001.56–133249.2 | ... | 23.16717 | −13.54746 | 19.678 | 18.752 | 18.128 | 18.221 | 18.5 | 0.06 | 0.004 | 0.002 | 0.003 | 0.013 | 0.039 | 1.6 | 1 | 0.94 | 1 |
| J230946.80–133547.0 | ... | 23.16301 | −13.59645 | 19.76 | 18.499 | 17.597 | 17.12 | 17.34 | 0.3 | 0.005 | 0.002 | 0.003 | 0.006 | 0.017 | 0.1 | 1 | 1 | 1 |
| J230944.28–132944.5 | ... | 23.16238 | −13.49577 | 20.445 | 19.572 | 18.854 | 18.374 | 18.521 | 0.17 | 0.01 | 0.005 | 0.008 | 0.016 | 0.042 | 0.3 | 1 | 1 | 1 |
| J230939.60–135751.1 | ... | 23.16135 | −13.96480 | 21.981 | 20.995 | 20.313 | 19.654 | 19.611 | 0.21 | 0.015 | 0.007 | 0.012 | 0.045 | 0.099 | 2.5 | 1 | 0.8 | 1 |
| J230919.08–132915.3 | ... | 23.15536 | −13.48751 | 20.279 | 19.534 | 18.984 | 18.898 | 19.151 | 0.51 | 0.006 | 0.003 | 0.005 | 0.024 | 0.067 | 0.5 | 1 | 1 | 1 |
| J230919.08–132354.9 | ... | 23.15526 | −13.39845 | 22.113 | 21.104 | 20.535 | 20.349 | – | 0.27 | 0.019 | 0.01 | 0.016 | 0.087 | – | 0.7 | 1 | 0.99 | 1 |
| J230916.20–132101.0 | ... | 23.15449 | −13.35043 | 19.775 | 18.915 | 18.294 | 18.285 | 18.601 | 0.23 | 0.003 | 0.002 | 0.003 | 0.013 | 0.04 | 0.4 | 1 | 1 | 1 |

Notes. The full catalogues of cross-matched sources for Abell 209 and Abell S295 are available online. Columns (1)–(11) list the radio source properties and are the same as Cols. (1)–(11) in the DR1 compact source catalogue presented in Table 2. Additional columns: (12) and (13) RA and Dec of DECaLS cross-match; (14) *g*-band magnitude; (15) *r*-band magnitude; (16) *z*-band magnitude; (17) WISE W1-band magnitude; (18) WISE W2-band magnitude; (19) Photometric redshift (see Sect. 8.2 for description; typical uncertainty $\delta z/(1+z) = 0.03$); (20)–(24) 1σ uncertainty on *g*, *r*, *z*, W1, and W2 magnitudes, respectively; (25) Angular separation between MGCLS source and optical match; (26) Match flag: 0 – no optical counterpart, 1 – the best optical counterpart according to the probabilities in Col. (28), 2 – the second-best optical counterpart according to the probabilities in Col. (28), etc.; (27) Probability that the MeerKAT source has a matched counterpart; (28) Probability that the MeerKAT source has the listed matched counterpart. In cases where there are more than one optical counterpart detected within $4''$, this column lists the probability of each of the objects being the optical counterpart. See Sect. 5.2.2 for details.

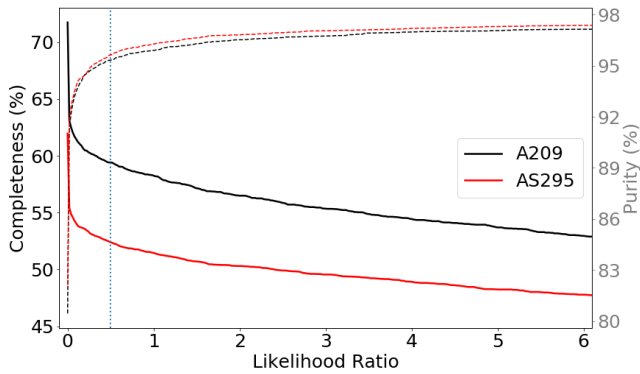


Fig. 6. Completeness (left axis, solid lines) and purity (right axis, dashed lines) versus the LR for Abell 209 (black) and Abell S295 (red). Imposing a LR cutoff at 0.5 (vertical dotted line) for Abell 209, the estimated spurious identification rate (error rate, or $1 - \text{purity}$) is 4.5%, with a completeness of 59%.

and is still typically done through visual inspection. Automated methods, such as those discussed in Appendix C, will be needed as our datasets become larger and larger. We visually inspected the Abell 209 and Abell S295 fields, finding 33 and 26 multi-component sources in each field, respectively. The largest of these multiple-component sources spans an angular size of $9.8'$. For each source we measured the integrated flux density, including all components, using pixels above 3σ , where σ is the local rms. Catalogues of these sources are presented in Tables A.1 and A.2, which include the likely optical or infrared counterpart from either the DECaLS or Wide-field Infrared Survey Explorer (WISE, Wright et al. 2010) catalogues. The catalogue position for each extended radio source is fixed to that of its likely optical or infrared counterpart, if available, or otherwise given by the flux-weighted centroid.

Due to the combination of high sensitivity and resolution, many well-resolved and multi-component radio galaxies have contaminating foreground or background sources that can currently only be separated visually, if at all. Figure 7 shows one example of a giant radio galaxy (Colafrancesco et al.

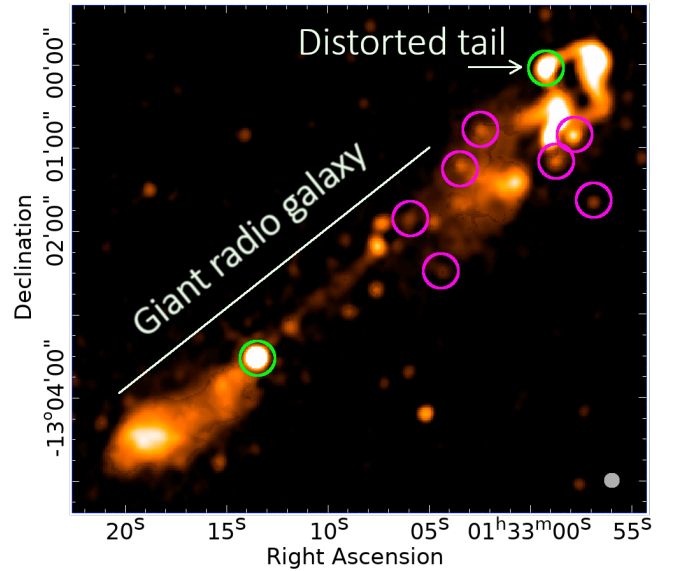


Fig. 7. Full-resolution ($7.6'' \times 7.4''$) MGCLS Stokes-*I* intensity image of a multi-host structure in the field of Abell 209. We indicate the two possible intersecting multi-component radio galaxies (giant radio galaxy and a distorted tailed galaxy). The compact radio components circled in green indicate the positions of the likely optical hosts, while the magenta circles indicate other superposed or nearby compact radio emission with optical counterparts. The brightness scale is logarithmic and saturates at 1 mJy beam^{-1} . The synthesised beam is indicated in the lower right corner.

2016; Kuźmicz et al. 2018) in the Abell 209 field. This $\sim 7.7'$ structure appears to have several possible optical or infrared counterparts, all of which are associated with compact radio features. The left-most green circle in Fig. 7 indicates the position of WISE J013313.50–130330.5, a candidate quasar (Flesch 2019) at a redshift of $z = 0.289$ and the likely counterpart for the giant radio galaxy. At that redshift, the radio galaxy extent would be $>1.5 \text{ Mpc}$. The right-most green circle is associated with WISE J013259.20–130002.0, which has no available

redshift. It appears to be a distorted bent-tail source whose features merge (in projection) with those of the western lobe of the assumed giant radio galaxy. Spectral index studies and redshift measurements will likely to be needed to disentangle such structures (Mhlahlo & Jamrozny 2021), which appear frequently in the MGCLS images, due to the high sensitivity to extended structures.

6. MGCLS diffuse cluster emission

A key aspect of radio observations of galaxy clusters is the detection of diffuse cluster-scale synchrotron emission, which carries information about the cluster formation history (see van Weeren et al. 2019; Brunetti & Jones 2014, for observational and theoretical reviews, respectively). There are several different categories of diffuse cluster radio emission, historically separated into three main classes: radio halos, mini-halos, and radio relics. All classes are characterised by low surface brightness and, typically, steep radio spectra ($\alpha \lesssim -1.1$).

Radio halos are diffuse sources that cover scales greater than 500 kpc, with many spanning megaparsec scales. They are typically seen to have morphologies closely linked to those of the X-ray emitting ICM. Both individual studies (e.g. Brunetti et al. 2001; Lindner et al. 2014) and statistical studies of large samples (Cassano et al. 2013; Kale et al. 2015; Cuciti et al. 2021a) have shown a strong link between radio halos and particle re-acceleration following major cluster mergers, as well as correlations between source radio power and cluster mass and thermal properties.

Radio mini-halos are found in the central region of dynamically relaxed, cool-core clusters (see Giacintucci et al. 2017, for a recent update). They are defined to be smaller than radio halos, with projected sizes ranging from a few tens of to a few hundred kiloparsecs, usually confined within cold fronts at the cluster centre (Mazzotta & Giacintucci 2008). Mini-halo clusters always have a radio active brightest cluster galaxy (BCG), which is thought to provide at least a fraction of the seed electrons necessary to produce the diffuse emission (see e.g. Richard-Laferrrière et al. 2020). Particle re-acceleration induced by gas sloshing is possibly the driving mechanism for mini-halos (e.g. ZuHone et al. 2011, 2013).

Radio relics are elongated megaparsec-scale structures located at the periphery of merging galaxy clusters. Their observed properties, which include a high degree of polarisation (see for instance the case of the Sausage cluster, van Weeren et al. 2010) are consistent with the idea that they are related to the presence of merger-induced shocks in the ICM. Double radio relics are found in a number of clusters, the prototype case being Abell 3667 (Rottgering et al. 1997), and in some cases a radio halo is detected as well (see e.g. Bonafede et al. 2012; Lindner et al. 2014). Radio phoenix sources are a subclass of relics thought to be related to revived fossil emission from radio AGN in the cluster region (van Weeren et al. 2019).

Radio halos and relics have been detected in an increasing number of merging clusters, over a broad range of cluster masses (see van Weeren et al. 2019; Cuciti et al. 2021b, for recent updates) and over a wide range of redshifts (Lindner et al. 2014; Di Gennaro et al. 2021). The detection of mini-halos, by contrast, remains limited, mainly due to observational constraints. In addition to the three main classes, more clusters with very steep-spectrum filaments have been detected recently (e.g. Abell 2034, Shimwell et al. 2016), requiring further investigation of the connection between the structures and particle reservoirs radio galaxies deposit into the ICM, and the

effects of cluster merger events (see e.g. van Weeren et al. 2017; de Gasperin et al. 2017).

Of the 115 clusters observed in this Legacy Survey, 62 have some form of diffuse cluster emission, with several clusters hosting more than one diffuse source. Table 4 presents the list of all 99 diffuse cluster structures or candidates detected in the survey. Fifty-six of these are new. For each diffuse source we list the emission classification, as well as angular and physical projected sizes, and position relative to cluster centre (where relevant). Classifications are based on a combined interrogation of the full- and 15'' resolution MeerKAT data products, a 25'' resolution filtered image (see Sect. 4.3.1 for details), and any available optical and X-ray imaging. Candidate structures are those with either marginal detections or where the classification is uncertain. Where a diffuse source does not fit into any of the current classes, but is not clearly associated with an individual radio galaxy, we classify it as 'unknown'. Our diffuse cluster emission detections can be summarised as follows: three new mini-halos and seven new mini-halo candidates, 27 halo detections and six candidates (of which 13 are new), 28 relics and 18 candidates (of which 26 are new), one known phoenix source and two new candidates, and nine diffuse sources, six of which are new, with ambiguous or unknown classifications.

The galaxy clusters observed in the MGCLS provide just a glimpse of the many diffuse cluster emission discoveries likely to be made in the Square Kilometre Array era. In the following, we present a few examples to show the much improved images compared to previous observations, opening up new areas of investigation, as well as discoveries highlighting specific interesting science issues. Flux densities for the diffuse emission in these systems have been measured by integrating the surface brightness within the 3σ contour in the 15'' resolution image and then subtracting the compact source contributions, which are determined from the full-resolution image. In some cases the 25'' resolution filtered image shows a greater extent to the diffuse structures than the 15'' resolution products; the flux densities quoted here may be considered as lower limits to the total amount of diffuse emission.

6.1. New insights into known sources

Twenty-eight of the MGCLS targets are hosts of previously known diffuse cluster emission. In many cases the MGCLS data provide an additional frequency or deeper detections of low-surface-brightness emission, yielding new insights into well-known sources (e.g. El Gordo, Abell 3376). Here we provide three examples.

6.1.1. Abell 85: A new type of halo?

The MGCLS multi-resolution view of the Abell 85 system, a cool-core cluster at $z = 0.0556$ and part of the Pisces-Cetus supercluster, is shown in the top panel of Fig. 8. We detect two diffuse sources: a complex phoenix or revived fossil plasma source south-west of the cluster centre (previously known) and a newly discovered elongated radio mini-halo that may be an example of a new class of sources that represents an evolutionary bridge between mini-halos and halos.

The newly detected diffuse source in Abell 85 surrounds the BCG, with contours shown in panel A of Fig. 8, and has a 1.28 GHz flux density of ~ 5.5 mJy measured from the 15'' resolution image. The 25'' resolution image, also shown in Fig. 8, reveals a much greater extent to this source, with a largest